Available online at www.sciencedirect.com
ScienceDirect
Journal of Computational Physics 225 (2007) 975–994
JOURNAL OF COMPUTATIONAL PHYSICS
www.elsevier.com/locate/jcp

A domain decomposition approach for non-conformal couplings between finite and boundary elements for unbounded electromagnetic problems in $\mathscr{R}^3$ ☆

Marinos Vouvakis [a], Kezhong Zhao [b,*], Seung-Mo Seo [b], Jin-Fa Lee [b]

[a] *Center for Advanced Communication and Sensor Antennas, Department of Electrical and Computer Engineering, University of Massachusetts, 215J Marcus Hall, 100 Natural Resources Rd., Amherst, MA 01003, United States*
[b] *The Ohio State University, Electrical Engineering, 1320 Kinnear Rd., Columbus, OH 43212, United States*

Received 8 August 2006; received in revised form 1 January 2007; accepted 3 January 2007
Available online 27 January 2007

Abstract

This paper presents a symmetric FEM–BEM formulation for solving unbounded three-dimensional electromagnetic problems. The approach is based on domain decomposition method that decomposes original problem into FEM and BEM domains. Two domains communicate through Robin transmission condition enforced on the interface between these two domains. The meshes on the interface are non-matching (non-conformal), thus two domains can be modularly treated. The resulting system matrix is symmetric and free of internal resonances. To accelerate the convergence of iterative solvers, three Schwarz type preconditioners are proposed. An ad hoc proof of convergence for the proposed Robin interface between FEM and BEM is also included for spherical outer boundaries. The efficiency and performance of the proposed approach with three different preconditioners are demonstrated through a few numerical examples.

Keywords: Domain decomposition method; Finite element method; Boundary element method; Electromagnetic radiation and scattering; Hybrid method; Computational electromagnetic; Maxwell equations

1. Introduction

To solve unbounded electromagetic problems in $\mathscr{R}^3$, a popular approach is to combine and couple the finite and boundary elements. Arguably, the hybrid Finite Elements–Boundary Elements Method (FE–BEM) has been one of the most successful methods to analyze unbounded electromagnetic radiation and scattering from heterogeneous structures [1–5]. The method combines FEM's versatility and robustness to model geometrically complex structures and materials and also the BEM's ability to efficiently and accurately deal with unbounded domains. However, widely used hybridizations of FEM and BEM [1–3,5] are

☆ This project is supported partially by AFOSR MURI Grant #FA9550-04-1-0359 and by Temasek Laboratories, Singapore.
* Corresponding author.
E-mail address: zhao.74@osu.edu (K. Zhao).

0021-9991/$ - see front matter
doi:10.1016/j.jcp.2007.01.014

based on non-variational settings that lead to non-symmetric complex system of equations, even when the actual physical problems involve only reciprocal media. In spite of that, such formulations have been successfully applied to both scattering and radiation problems, even though they do not reflect the reciprocal nature of the physical problems. It is the authors' belief that it is desirable for numerical methods to result in symmetric matrix equations when dealing with electromagnetic problems with only reciprocal materials. Furthermore, the non-variational formulations are usually more difficult and more computationally expensive to solve with iterative solvers. The symmetric coupling between finite and boundary elements was first proposed by Costabel [6] in 1987. Since then, quite a few papers have been published on the topic of symmetric couplings. In [7], Hiptmair describes the Costabel's approach as the use of weak exterior Calderon projector to furnish the needed Dirichlet-to-Neumann mapping for the couplings. Subsequently, he [7] extended the symmetric couplings to analyze electromagnetic eddy current problems where the displacement currents are negligible. For electromagnetic wave radiation and scattering problems, the symmetric couplings between finite and boundary elements have been developed by Hiptmair [8], Vouvakis et al. [9] and Lee et al. [10]. These approaches attempt a variational symmetric enforcement of the Dirichlet-to-Neumann map between FEM and BEM; consequently, without any special treatment, they suffer the infamous internal resonance or "forbidden" frequency problem [8,10]. This issue of internal resonances in the symmetric Dirichlet-to-Neumann mapping has been pointed out explicitly and proved by Hiptmair in [8] and numerically demonstrated by Lee et al. in [10]. It should be emphasized that the non-variational approaches of [1–3,5] do not suffer internal resonances only if the combined-field integral equation (CFIE) is used on the BEM portion.

On the other hand, both aforementioned variational and non-variational formulations lack modularity. Namely, FEM and BEM have to be consistent with each other in terms of mesh and basis functions. Modular FEM–BEM hybrid formulations have been previously proposed for two-dimensional problems by Cwik in [11] and Hoppe et al. in [4] for body-of-revolution problems. In both cases different FEM and BEM meshes were used leading to memory savings due to the reduced mesh density of the boundary element part. Finally, to the authors' best knowledge, an effective and efficient preconditioning scheme that guarantees convergence of the FEM–BEM system is yet to be found. Here it is worth mentioning the work of Liu et al. [12] and Stupfel in [13]. In the former work an effective preconditioner for a non-variational FEM–BEM coupling was proposed. The important ingredients in that preconditioning approach were the use of the Robin-boundary conditions and domain overlapping between FEM and BEM. In the latter case, domain decomposition based FEM was coupled to a BEM formulation also using the Robin transmission condition, but without overlapping. The overall statement of the problem leads to a non-symmetric system that was solved using a stationary outer loop iteration scheme.

The present method is a continuation of [9] that will address and alleviate each of the aforementioned issues. Similar to [9], the proposed approach is variational, thus results in a symmetry system matrix. Unlike [9], it almost decouples FEM and BEM as two independent computational domains, inspired by Lee et al. [14] previous work on the non-conforming and non-overlapping domain decomposition method. Consequently, both FEM and BEM domains can be modularly treated in terms of meshing, selection of basis functions, matrix assembling, even solution process. The ability of the proposed formulation to combine different orders and/or types of basis functions and different iterative or direct solvers on the FEM and BEM parts significantly simplifies the integration of already existing off-the-shelf FEM and BEM implementations into the hybrid. Moreover, the non-conformal meshes between FEM and BEM tremendously relax the computational burden of BEM, especially when *h*-adaptive mesh refinement strategies [15] are considered. Additionally, the modular nature of the proposed DD–FE–BEM coupling could pay significant dividend in parallel versions of the method. The present method is free of internal resonances because the FEM part is based on FEM-ABC (finite element method with absorbing boundary condition), whereas the BEM part employs a combined-field integral equation formulation (CFIE) and the coupling utilizes the Robin-to-Robin map instead of the Dirichlet-to-Neumann map. The FEM-ABC formulation admits only complex frequency resonances since it represents a lossy cavity. Meanwhile, the Robin-to-Robin map is a communication mechanism across the FEM and BEM interface that allows for the enforcement of both electric and magnetic field continuities, such that any resonance condition would occur only at complex frequencies. Apart from solving the internal resonance problem, the use of Robin transmission condition improves the convergence of the overall iterative solution and when

combined with appropriate preconditioning schemes it leads to fast convergence in the iterative matrix solution process. In the solution stage the present method utilizes a preconditioned conjugate gradient solver since the matrix is symmetric and the real part of all eigenvalues of the preconditioned matrix are positive. In summary, the proposed hybrid offers simultaneously: (1) symmetry, (2) modularity, (3) non-conformity between FEM and BEM domains, (4) free of internal resonance and (5) natural and effective preconditioning schemes, which assure the convergence of propagating modes.

Before proceeding into the outline of the paper it is noted that the fast solution methods and reduction of the heavy computational burden of a full BEM approach will not be discussed in this paper. We refer the interested readers to Refs. [16–19]. It is sufficient to state that, the method has been integrated with both Adaptive Cross Approximation (ACA) method [18,17] and the Integral Equation Fast Fourier Transform (IE-FFT) method [19].

The rest of this paper is planned as follows. A boundary value problem (BVP) in terms of the "cement" variables is described in Section 2 for the Maxwell equations in $\mathscr{R}^3$. Section 3 discusses the representation formulae and the exterior Calderon projector; while Section 4 is the technical core of the paper, which details the Galerkin variational statement, the proper function spaces and the discrete coupling mechanisms; the final matrix equation is then outlined in Section 5 and the symmetric nature of the DD–FE–BEM is also emphasized. Section 6 provides an insightful and physical description of the proposed DD–FE–BEM and the nature of the couplings is analyzed through a simplified spherical boundary truncation; Three preconditioning schemes are proposed in Section 7. Numerical results are included in Section 8, which validate the spectral radius of the coupling matrix blocks and demonstrate an interesting feature in terms of convergence rate for the non-conforming nature of the proposed method. Moreover, in Section 8 we compared the performances of three preconditioners for solving real-life engineering applications; and, Finally, a short and brief conclusion is provided in Section 9.

2. Boundary value problems

This paper considers the solutions of electromagnetic radiation and scattering problems in $\mathscr{R}^3$. However, in order to make our presentation concise herein, we limit our discussions on only the scattering problems. Minor modifications are needed to extend current formulation to radiation type problems.

A finite computational domain, $\Omega \subset \mathscr{R}^3$, encloses all the scatterers inside. The exterior region, $\Omega^c = \mathscr{R}^3/\overline{\Omega}$, is then homogeneous and assumed to be free space. Let $\mathbf{E}$ denotes the scattered electric field in the exterior region Ω^c and the total electric field inside Ω. It is then the solution of the following transmission problem [8]:

$$\begin{aligned}
&\nabla \times \nabla \times \mathbf{E} - k^2 \mathbf{E} = 0 \quad \text{in } \Omega^c \\
&\nabla \times \frac{1}{\mu_r} \nabla \times \mathbf{E} - k^2 \epsilon_r \mathbf{E} = 0 \quad \text{in } \Omega \\
&[\gamma_t \mathbf{E}]_\Gamma = -\gamma_t \mathbf{E}^{\text{inc}}, \ [\gamma_N \mathbf{E}]_\Gamma = -\gamma_N \mathbf{E}^{\text{inc}} \quad \text{on } \Gamma \\
&\lim_{|\mathbf{x}| \to \infty} \nabla \times \mathbf{E} \times \mathbf{x} - \mathrm{i}k|\mathbf{x}|\mathbf{E} = 0
\end{aligned} \tag{2.1}$$

In (2.1), k is the wavenumber in free space, two surface trace operators are $\gamma_t \mathbf{E} = \mathbf{n} \times \mathbf{E} \times \mathbf{n}|_\Gamma$ for the tangential components of $\mathbf{E}$ on Γ and $\gamma_N \mathbf{E} = \frac{1}{k} \nabla \times \mathbf{E} \times \mathbf{n}|_\Gamma$ for the "magnetic trace" on Γ. We should remark here that the "magnetic trace" is closely related to the surface "electric current". Also, throughout this paper, the superscripts $-$ and $+$ tag traces onto Γ from Ω and Ω^c, respectively. Another trace operator that we shall encounter later is the twisted surface trace, viz. $\gamma_\times \mathbf{u} = \mathbf{u} \times \mathbf{n}$. The surface unit normal $\mathbf{n}$ points from Ω toward the exterior region Ω^c (as indicated in Fig. 1) and $[\gamma\phi]_\Gamma = \gamma\phi|_{\Omega^c} - \gamma\phi|_\Omega = \gamma^+\phi - \gamma^-\phi$ denotes the jump of a function ϕ across Γ. We have also imposed the Silver–Müller radiation condition for the scattered field in the exterior region Ω^c as $\mathbf{x} \to \infty$.

The current formulation starts by introducing two "cement" variables [14], $\mathbf{j}^-$ and $\mathbf{j}^+$, on the boundary Γ. These two cement variables are the magnetic traces on Γ^- and Γ^+, respectively. Namely, $\mathbf{j}^- = \gamma_N^- \mathbf{E}$ and $\mathbf{j}^+ = -\gamma_N^+ \mathbf{E}$. Subsequently, the original transmission problem (2.1) can be stated alternatively as Dirichlet and Neumann couplings in Ω

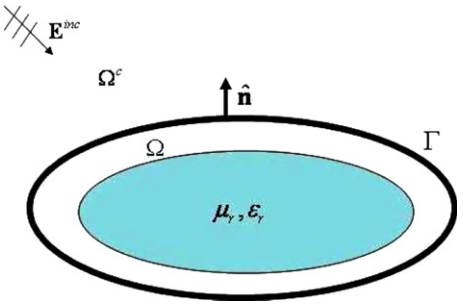

Fig. 1. An electromagnetic scattering problem in 3D.

$$\nabla \times \frac{1}{\mu_r} \nabla \times \mathbf{E} - k^2 \epsilon_r \mathbf{E} = 0 \tag{2.2}$$

$$\frac{1}{\mu_r} \gamma_N^- \mathbf{E} = \mathbf{j}^- \quad \text{in } \Omega^c$$

$$\nabla \times \nabla \times \mathbf{E} - k^2 \mathbf{E} = 0$$

$$\lim_{|\mathbf{x}| \to \infty} \nabla \times \mathbf{E} \times \mathbf{x} - \mathrm{i}k|\mathbf{x}|\mathbf{E} = 0 \tag{2.3}$$

$$-\gamma_N^+ \mathbf{E} = \mathbf{j}^+$$

Transmission conditions on Γ

$$\begin{aligned} \mathbf{e}^- - \mathbf{e}^+ &= \gamma_t \mathbf{E}^{\text{inc}} \\ \mathbf{j}^- + \mathbf{j}^+ &= \gamma_N \mathbf{E}^{\text{inc}} \end{aligned} \tag{2.4}$$

with $\mathbf{e}^{\pm} = \gamma_t^{\pm} \mathbf{E}$. However, direct numerical implementation based on the transmission conditions (2.4) is not desirable since they are closely related to the Dirichlet and Neumann type boundary conditions, which usually subject the sub-domains to the "internal resonances" during the solution process. Taking our cue from the domain decomposition literature, we simply replace (2.4) by Robin-type transmission condition [14]. They are Robin-type couplings

$$\begin{aligned} -\mathrm{i}\mathbf{e}^- + \mathbf{j}^- &= -\mathrm{i}\mathbf{e}^+ - \mathbf{j}^+ + \mathbf{f}^{\text{inc}} \\ -\mathrm{i}\mathbf{e}^+ + \mathbf{j}^+ &= -\mathrm{i}\mathbf{e}^- - \mathbf{j}^- - \mathbf{g}^{\text{inc}} \end{aligned} \tag{2.5}$$

where $\mathbf{f}^{\text{inc}} = -\mathrm{i}\gamma_t \mathbf{E}^{\text{inc}} + \gamma_N \mathbf{E}^{\text{inc}}$ and $\mathbf{g}^{\text{inc}} = -\mathrm{i}\gamma_t \mathbf{E}^{\text{inc}} - \gamma_N \mathbf{E}^{\text{inc}}$. We remark that in the continuous problem, the Robin-type transmission conditions (2.5) are equivalent to those of (2.4). However, different transmission conditions result in different characteristics in the final matrix equations. Particularly, the spectral radius of the couplings between finite elements and boundary elements. We shall elaborate on this issue in more detail later.

3. Representation formulae in Ω^c and the Calderon projector

In this section, we start with the vector wave equation in the exterior region Ω^c, where μ and ϵ are simply μ_0 and ϵ_0. We begin by stating that if $\mathbf{u}$ is a Maxwell solution in the exterior region Ω^c that satisfies the Silver–Müller radiation condition at infinity, then it can be expressed as [20]

$$\mathbf{u}(\mathbf{x}) = -\Psi_{\text{DL}}^k(\gamma_\times^+ \mathbf{u})(\mathbf{x}) - \Psi_{\text{SL}}^k(\gamma_N^+ \mathbf{u})(\mathbf{x}), \quad \mathbf{x} \in \Omega^c \tag{3.1}$$

where

$$\Psi_{\text{SL}}^k(\mathbf{u})(\mathbf{x}) := k\Psi_{\mathbf{A}}^k(\mathbf{u})(\mathbf{x}) + \frac{1}{k} \nabla \Psi_V^k (\nabla_\Gamma \cdot \mathbf{u})(\mathbf{x}), \quad \mathbf{x} \notin \Gamma$$

$$\Psi_{\text{DL}}^k(\mathbf{u})(\mathbf{x}) := \nabla \times \Psi_{\mathbf{A}}^k(\mathbf{u})(\mathbf{x}), \quad \mathbf{x} \notin \Gamma$$

with the single-layer scalar, Ψ_V^k and vector, $\Psi_{\mathbf{A}}^k$, potentials defined by

$$\Psi_V^k(\phi)(\mathbf{x}) := \int_\Gamma \phi(\mathbf{y}) g(\mathbf{x}-\mathbf{y}) \mathrm{d}S_\mathbf{y}, \quad \Psi_\mathbf{A}^k(\mathbf{u})(\mathbf{x}) := \int_\Gamma \mathbf{u}(\mathbf{y}) g(\mathbf{x}-\mathbf{y}) \mathrm{d}S_\mathbf{y} \tag{3.2}$$

where $g(\mathbf{x}-\mathbf{y}) = \frac{e^{ik|\mathbf{x}-\mathbf{y}|}}{4\pi|\mathbf{x}-\mathbf{y}|}$ is the kernel of the scalar Helmholtz equation. In Ref. [8], Ψ_{SL}^k and Ψ_{DL}^k are called the Maxwell single-layer and double-layer potentials, respectively.

Taking curl of Eq. (3.1) results in

$$\nabla \times \mathbf{u}(\mathbf{x}) = -\nabla \times \Psi_{\mathrm{DL}}^k\left(\gamma_\times^+ \mathbf{u}\right)(\mathbf{x}) - \nabla \times \Psi_{\mathrm{SL}}^k\left(\gamma_N^+ \mathbf{u}\right)(\mathbf{x}) \tag{3.3}$$

Yet, due to the fact that $\nabla \times \Psi_{\mathrm{SL}}^k = k\Psi_{\mathrm{DL}}^k$ and $\nabla \times \Psi_{\mathrm{DL}}^k = k\Psi_{\mathrm{SL}}^k$, we have

$$\frac{1}{k}\nabla \times \mathbf{u}(\mathbf{x}) = -\Psi_{\mathrm{SL}}^k\left(\gamma_\times^+ \mathbf{u}\right)(\mathbf{x}) - \Psi_{\mathrm{DL}}^k\left(\gamma_N^+ \mathbf{u}\right)(\mathbf{x}) \tag{3.4}$$

Hence the Dirichlet and Neumann traces of the surface field, $\mathbf{u}$, on the exterior surface, Γ^+, can be written as

$$\begin{aligned} \gamma_\times^+ \mathbf{u}(\mathbf{x}) &= -\gamma_\times^+ \Psi_{\mathrm{DL}}^k\left(\gamma_\times^+ \mathbf{u}\right)(\mathbf{x}) - \gamma_\times^+ \Psi_{\mathrm{SL}}^k\left(\gamma_N^+ \mathbf{u}\right)(\mathbf{x}) \\ \gamma_N^+ \mathbf{u}(\mathbf{x}) &= -\gamma_\times^+ \Psi_{\mathrm{SL}}^k\left(\gamma_\times^+ \mathbf{u}\right)(\mathbf{x}) - \gamma_\times^+ \Psi_{\mathrm{DL}}^k\left(\gamma_N^+ \mathbf{u}\right)(\mathbf{x}) \end{aligned} \tag{3.5}$$

Moreover, we have

$$\gamma_\times^+ \Psi_{\mathrm{DL}}^k = -\frac{Id}{2} + \{\gamma_\times\}\Psi_{\mathrm{DL}}^k, \quad \{\gamma_\times\} = \frac{\gamma_\times^+ + \gamma_\times^-}{2} \tag{3.6}$$

Eq. (3.6) is the direct consequence of the properties of the Maxwell single-layer and double-layer potentials [8], namely

$$\left[\gamma_\times \Psi_{\mathrm{SL}}^k\right] = \left[\gamma_N \Psi_{\mathrm{DL}}^k\right] = 0, \quad \left[\gamma_N \Psi_{\mathrm{SL}}^k\right] = \left[\gamma_\times \Psi_{\mathrm{DL}}^k\right] = -Id \tag{3.7}$$

Substituting Eq. (3.6) into (3.5) results in

$$\begin{aligned} \gamma_\times^+ \mathbf{u} &= \frac{1}{2}\gamma_\times^+ \mathbf{u} - \{\gamma_\times\}\Psi_{\mathrm{DL}}^k\left(\gamma_\times^+ \mathbf{u}\right) - \{\gamma_\times\}\Psi_{\mathrm{SL}}^k\left(\gamma_N^+ \mathbf{u}\right) \\ \gamma_N^+ \mathbf{u} &= -\{\gamma_\times\}\Psi_{\mathrm{SL}}^k\left(\gamma_\times^+ \mathbf{u}\right) + \frac{1}{2}\gamma_N^+ \mathbf{u} - \{\gamma_\times\}\Psi_{\mathrm{DL}}^k\left(\gamma_N^+ \mathbf{u}\right) \end{aligned} \tag{3.8}$$

In a more compact form, Eq. (3.8) can be expressed in the matrix form as

$$\begin{pmatrix} \gamma_\times^+ \mathbf{u} \\ \gamma_N^+ \mathbf{u} \end{pmatrix} = \begin{pmatrix} \frac{Id}{2} - C_k & -S_k \\ -S_k & \frac{Id}{2} - C_k \end{pmatrix} \begin{pmatrix} \gamma_\times^+ \mathbf{u} \\ \gamma_N^+ \mathbf{u} \end{pmatrix} \tag{3.9}$$

where the operators are

$$\begin{aligned} S_k &:= \{\gamma_\times\}\Psi_{\mathrm{SL}}^k, \quad \mathbf{H}^{-1/2}(\mathrm{div}_\Gamma; \Gamma) \mapsto \mathbf{H}^{-1/2}(\mathrm{div}_\Gamma; \Gamma) \\ C_k &:= \{\gamma_\times\}\Psi_{\mathrm{DL}}^k, \quad \mathbf{H}^{-1/2}(\mathrm{div}_\Gamma; \Gamma) \mapsto \mathbf{H}^{-1/2}(\mathrm{div}_\Gamma; \Gamma) \end{aligned} \tag{3.10}$$

Lastly, we note that since the exterior Calderon projector is a projector, it offers the following well-known identity:

$$\begin{pmatrix} \frac{Id}{2} - C_k & -S_k \\ -S_k & \frac{Id}{2} - C_k \end{pmatrix} \begin{pmatrix} \frac{Id}{2} - C_k & -S_k \\ -S_k & \frac{Id}{2} - C_k \end{pmatrix} \begin{pmatrix} \mathbf{u} \\ \mathbf{v} \end{pmatrix} = \begin{pmatrix} \frac{Id}{2} - C_k & -S_k \\ -S_k & \frac{Id}{2} - C_k \end{pmatrix} \begin{pmatrix} \mathbf{u} \\ \mathbf{v} \end{pmatrix} \tag{3.11}$$

for any surface tangent fields $\mathbf{u}$ and $\mathbf{v}$. Consequently, we have

$$\begin{pmatrix} \frac{Id}{2} - C_k & -S_k \\ -S_k & \frac{Id}{2} - C_k \end{pmatrix} \begin{pmatrix} \frac{Id}{2} - C_k & -S_k \\ -S_k & \frac{Id}{2} - C_k \end{pmatrix} = \begin{pmatrix} \frac{Id}{2} - C_k & -S_k \\ -S_k & \frac{Id}{2} - C_k \end{pmatrix} \Rightarrow \begin{cases} C_k C_k + S_k S_k = \frac{Id}{4} \\ S_k C_k + C_k S_k = 0 \end{cases} \tag{3.12}$$

4. Galerkin variational formulation

4.1. Function spaces

From the physical consideration that both the electric and magnetic energies of the system need be finite, it is transparent to see that the vector field $\mathbf{E}$ in Eq. (2.1) resides in the product space $\mathbf{H}(\mathrm{curl};\Omega)\times\mathbf{H}_{\mathrm{loc}}(\mathrm{curl};\Omega^{\mathrm{c}})$ [8]. To establish the proper spaces of the tangential traces $\mathbf{e}^-$, $\mathbf{e}^+$ as well as the cement variables $\mathbf{j}^-$ and $\mathbf{j}^+$, we borrow heavily from [8] for the following results:

Theorem 4.1. *The trace mappings* $\gamma_t^+ : \mathbf{H}_{\mathrm{loc}}(\mathrm{curl};\Omega^{\mathrm{c}})\mapsto\mathbf{H}^{-1/2}(\mathrm{curl}_\Gamma;\Gamma^+)$, $\gamma_t^- : \mathbf{H}(\mathrm{curl};\Omega)\mapsto\mathbf{H}^{-1/2}(\mathrm{curl}_\Gamma;\Gamma^-)$, $\gamma_\times^+ : \mathbf{H}_{\mathrm{loc}}(\mathrm{curl};\Omega^{\mathrm{c}})\mapsto\mathbf{H}^{-1/2}(\mathrm{div}_\Gamma;\Gamma^+)$, $\gamma_\times^- : \mathbf{H}(\mathrm{curl};\Omega)\mapsto\mathbf{H}^{-1/2}(\mathrm{div}_\Gamma;\Gamma^-)$ *are continuous and surjective. Moreover, the traces* $\gamma_N^\pm$ *furnish continuous mappings*: $\gamma_N^+ : \mathbf{H}_{\mathrm{loc}}(\mathrm{curl}^2;\Omega^{\mathrm{c}})\mapsto\mathbf{H}^{-1/2}(\mathrm{div}_\Gamma;\Gamma^+)$ *and* $\gamma_N^- : \mathbf{H}(\mathrm{curl}^2;\Omega)\mapsto\mathbf{H}^{-1/2}(\mathrm{div}_\Gamma;\Gamma^-)$.

Therefore, the proper spaces for the vector fields are

$$\begin{aligned}&\mathbf{E}\in\mathbf{H}(\mathrm{curl},\Omega)\times\mathbf{H}_{\mathrm{loc}}(\mathrm{curl},\Omega^{\mathrm{c}})\\&\mathbf{e}^\pm\in\mathbf{H}^{-1/2}(\mathrm{curl}_\Gamma,\Gamma^\pm)\\&\mathbf{j}^\pm\in\mathbf{H}^{-1/2}(\mathrm{div}_\Gamma,\Gamma^\pm)\end{aligned}\tag{4.1}$$

Now we are ready to state the variational formulation which couples the finite and boundary elements on non-conformal meshes. By non-conformity, we refer to the fact that the triangulation on Γ^- need not be the same as the triangulation on Γ^+. This non-conformity feature admits two major benefits: (a) Different orders of polynomial approximations can be employed separately for finite elements and boundary elements. This is particularly relevant in the BEM portion of discretization. Since both first and second kind of integral equations are needed in the BEM formulation, higher order basis functions will demand significant efforts to achieve high accuracy in the numerical integrations for evaluating weak- and hyper-singular integrals. For simplicity, we employed only the lowest order Raviart–Thomas [21] or RWG [22] basis functions for the BEM implementation. Whereas in the FEM implementation, exact integrations can be performed for straight-sided tetrahedra even with high-order Nédélec elements, therefore, we are using $p=2$ mixed Nédélec elements [23]; and (b) In the process of goal-oriented adaptive mesh refinements [15], the triangulation on Γ^- often become un-necessary small in certain regions for the boundary elements. The non-conformal coupling approach allows for a more uniform triangulation on Γ^+ and hence can greatly reduce the computational burden.

4.2. Variational formulation for the interior region Ω

Given a surface trace field $\mathbf{j}^-(\equiv\frac{1}{k}\nabla\times\mathbf{E}\times\mathbf{n})\in\mathbf{H}^{-1/2}(\mathrm{div}_\Gamma;\Gamma^-)$ the corresponding variational statement of (2.1) for the interior region Ω is

$$\text{Seek } \mathbf{E}\in\mathbf{H}(\mathrm{curl};\Omega) \text{ such that } \mathscr{A}(\mathbf{v},\mathbf{E})_\Omega - k\left\langle\gamma_t^-\mathbf{v},\mathbf{j}^-\right\rangle_{\Gamma^-}=0\quad\forall\mathbf{v}\in\mathbf{H}(\mathrm{curl};\Omega)\tag{4.2}$$

with $\mathscr{A}(\mathbf{v},\mathbf{E})_\Omega=\int_\Omega\left[\nabla\times\mathbf{v}\cdot\frac{1}{\mu_r}\nabla\times\mathbf{E}-k^2\mathbf{v}\cdot\epsilon_r\mathbf{E}\right]\mathrm{d}V$ and $\langle\beta,\lambda\rangle_{\Gamma^\pm}=\int_{\Gamma^\pm}(\beta\cdot\lambda)\mathrm{d}S$. The finite element application involves a finite-dimensional approximation of (4.2). We suppose that Ω has been covered by a regular, non-uniform mesh Ω^h (resulted from goal-oriented h-version adaptive mesh refinements [15]), consisting of tetrahedra. We write

$$\Omega^h=\bigcup_m T_m^{h_m}\tag{4.3}$$

where $T_m^{h_m}$ denotes the mth tetrahedral element in the mesh Ω^h. Moreover, the superscript h_m indicates the diameter of the tetrahedron T_m. Subsequently, the finite-dimensional subspaces employed for the interior finite elements are

$$\begin{aligned}&\mathscr{X}_h=\left\{\mathbf{v}\in\mathbf{H}(\mathrm{curl};\Omega):\mathbf{v}|_T\in\mathscr{ND}_2^1(T)\ \forall T\in\Omega^h\right\}\\&\mathscr{W}_h^-=\left\{\lambda^-\in\mathbf{H}^{-1/2}(\mathrm{div}_\Gamma;\Gamma^-):\lambda^-|_\Delta\in\mathscr{RT}_2(\Delta)\ \forall\Delta\in\mathscr{D}_h^-\right\}\end{aligned}\tag{4.4}$$

where $\mathscr{ND}_2^1(T)$ denotes the $p=2$, first kind Nédélec family finite elements on tetrahedra. Note that the superscript 1 describes the first family of Nédélec elements (mixed Nédélec elements) [23], whereas the subscript 2 denotes the order of the polynomial space. Similarly, $\mathscr{RT}_2(\Delta)$ represents the $p=2$ Raviart–Thomas div-conforming elements on triangle Δ [21]. Furthermore, the surface triangulation is defined by $\mathscr{D}_h^- = \Omega_h|_{\Gamma^-}$.

Given a $\mathbf{j}_h^- \in \mathscr{W}_h^-$, the finite element analogue of (4.2) is to

$$\text{Seek } \mathbf{E}_h \in \mathscr{X}_h \text{ such that } \mathscr{A}(\mathbf{v}_h, \mathbf{E}_h)_{\Omega_h} - k\langle \gamma_t^- \mathbf{v}_h, \mathbf{j}_h^- \rangle_{\mathscr{D}_h^-} = 0 \quad \forall \mathbf{v}_h \in \mathscr{X}_h \tag{4.5}$$

Moreover, let $\mathscr{V}_h^-$ denote the finite-dimensional space for all the surface trace fields, $\gamma_t^- \mathbf{v}_h$ with $\mathbf{v}_h \in \mathscr{X}_h$. That is $\mathscr{V}_h^- = \{\gamma_t^- \mathbf{v}_h | \mathbf{v}_h \in \mathscr{X}_h\}$ and we simply write $\mathscr{V}_h^- = \mathscr{X}_h|_{\Gamma^-}$.

4.3. Variational statement for the boundary elements

Starting with the exterior Calderon projector in (3.9) and taking $\mathbf{n}\times$ the first equation of (3.9), we have

$$\begin{aligned} \gamma_t^+ \mathbf{u} &= \frac{1}{2}\gamma_t^+ \mathbf{u} - \mathscr{B}_k(\gamma_\times^+ \mathbf{u}) - \mathscr{N}_k(\gamma_N^+ \mathbf{u}) \\ \gamma_N^+ \mathbf{u} &= \frac{1}{2}\gamma_N^+ \mathbf{u} - \mathscr{S}_k(\gamma_\times^+ \mathbf{u}) - \mathscr{C}_k(\gamma_N^+ \mathbf{u}) \end{aligned} \tag{4.6}$$

where $\mathscr{B}_k(\mathbf{u}) = \{\gamma_t\}\Psi_{\mathrm{DL}}^k(\mathbf{u})$ and $\mathscr{N}_k(\mathbf{u}) = \{\gamma_t\}\Psi_{\mathrm{SL}}^k(\mathbf{u})$. We remark that $\mathbf{n}\times\mathscr{C}_k = \mathscr{B}_k$ and $\mathbf{n}\times\mathscr{S}_k = \mathscr{N}_k$. Accordingly, the variational formulation for (4.6) can be stated as

$$\text{Seek } \mathbf{e}^+ \in \mathbf{H}^{-1/2}(\mathrm{curl}_\Gamma; \Gamma^+) \text{ and } \mathbf{j}^+ \in \mathbf{H}^{-1/2}(\mathrm{div}_\Gamma; \Gamma^+) \text{ such that}$$

$$\langle \lambda^+, \mathbf{e}^+ \rangle_{\Gamma^+} = \frac{1}{2}\langle \lambda^+, \mathbf{e}^+ \rangle_{\Gamma^+} - \langle \lambda^+, \mathscr{B}_k(\mathbf{e}^+ \times \mathbf{n}) \rangle_{\Gamma^+} + \langle \lambda^+, \mathscr{N}_k(\mathbf{j}^+) \rangle_{\Gamma^+} \tag{4.7}$$

$$\langle \beta^+, \mathbf{j}^+ \rangle_{\Gamma^+} = \frac{1}{2}\langle \beta^+, \mathbf{j}^+ \rangle_{\Gamma^+} + \langle \beta^+, \mathscr{S}_k(\mathbf{e}^+ \times \mathbf{n}) \rangle_{\Gamma^+} - \langle \beta^+, \mathscr{C}_k(\mathbf{j}^+) \rangle_{\Gamma^+} \tag{4.8}$$

$$\forall \beta^+ \in \mathbf{H}^{-1/2}(\mathrm{curl}_\Gamma; \Gamma^+) \text{ and } \lambda^+ \in \mathbf{H}^{-1/2}(\mathrm{div}_\Gamma; \Gamma^+)$$

Note that in writing (4.7) and (4.8), we have employed $\mathbf{j}^+ = -\gamma_N^+ \mathbf{E}$. Once more, we assume that Γ^+ is covered by a regular triangulation $\mathscr{D}_h^+$ with the maximum diameter h of all the triangles. Note that in our formulation, the triangulations $\mathscr{D}_h^- (= \Omega_h|_{\Gamma^-})$ and $\mathscr{D}_h^+$ do not need to be conformal. As mentioned previously, this feature of mesh non-conformity allows potential big savings in computer resources for many real-life complex problems. Moreover, the finite-dimensional subspaces that we employed for the surface traces are

$$\begin{aligned} \mathbf{e}_h^+ &\in \mathscr{V}_h = \left\{ \mathbf{v}_h \in \mathbf{H}^{-1/2}(\mathrm{curl}_\Gamma; \Gamma^+), \mathbf{v}_h|_\Delta \in \mathscr{ND}_1^1(\Delta)\ \forall \Delta \in \mathscr{D}_h^+ \right\} \\ \mathbf{j}_h^+ &\in \mathscr{W}_h = \left\{ \lambda_h^+ \in \mathbf{H}^{-1/2}(\mathrm{div}_\Gamma; \Gamma^+), \lambda_h^+|_\Delta \in \mathscr{RT}_1(\Delta)\ \forall \Delta \in \mathscr{D}_h^+ \right\} \end{aligned} \tag{4.9}$$

Note that we have utilized only the lowest order, namely $p=1$, elements for both the curl and div-conforming basis functions for $\mathbf{e}_h^+$ and $\mathbf{j}_h^+$, respectively. Again, the capability of choosing different orders of basis functions for the boundary elements regardless of the finite elements employed within the interior region is a very welcoming feature in addressing industrial applications. Before closing this subsection, we summarize the final Galerkin statement for the boundary elements. And, it is

$$\text{Seek } \mathbf{e}_h^+ \in \mathscr{V}_h^+ \text{ and } \mathbf{j}_h^+ \in \mathscr{W}_h^+ \text{ such that}$$

$$\begin{aligned} \langle \lambda_h^+, \mathbf{e}_h^+ \rangle_{\mathscr{D}_h^+} &= \frac{1}{2}\langle \lambda_h^+, \mathbf{e}_h^+ \rangle_{\mathscr{D}_h^+} - \langle \lambda_h^+, \mathscr{B}_k(\mathbf{e}_h^+ \times \mathbf{n}) \rangle_{\mathscr{D}_h^+} + \langle \lambda_h^+, \mathscr{N}_k(\mathbf{j}_h^+) \rangle_{\mathscr{D}_h^+} \\ \langle \beta_h^+, \mathbf{j}_h^+ \rangle_{\mathscr{D}_h^+} &= \frac{1}{2}\langle \beta_h^+, \mathbf{j}_h^+ \rangle_{\mathscr{D}_h^+} + \langle \beta_h^+, \mathscr{S}_k(\mathbf{e}_h^+ \times \mathbf{n}) \rangle_{\mathscr{D}_h^+} - \langle \beta_h^+, \mathscr{C}_k(\mathbf{j}_h^+) \rangle_{\mathscr{D}_h^+} \\ &\forall \beta_h^+ \in \mathscr{V}_h^+ \text{ and } \lambda_h^+ \in \mathscr{W}_h^+ \end{aligned} \tag{4.10}$$

4.4. Variational formulation for the Robin-type transmission conditions

We state the variational formulation for the Robin-type transmission conditions proposed in (2.5) as follows:

Seek $\mathbf{e}^{\pm} \in \mathbf{H}^{-1/2}(\mathrm{curl}_{\Gamma}; \Gamma^{\pm})$ and $\mathbf{j}^{\pm} \in \mathbf{H}^{-1/2}(\mathrm{div}_{\Gamma}; \Gamma^{-})$ such that

$$\langle \beta^-, \mathbf{j}^- \rangle_{\Gamma^-} - \mathrm{i}\langle \beta^-, \mathbf{e}^- \rangle_{\Gamma^-} = -\langle \beta^-, \mathbf{j}^+ \rangle_{\Gamma^-} - \mathrm{i}\langle \beta^-, \mathbf{e}^+ \rangle_{\Gamma^-} + \langle \beta^-, \mathbf{f}^{\mathrm{inc}} \rangle_{\Gamma^-} \tag{4.11}$$

$$\langle \lambda^-, \mathbf{j}^- \rangle_{\Gamma^-} - \mathrm{i}\langle \lambda^-, \mathbf{e}^- \rangle_{\Gamma^-} = -\langle \lambda^-, \mathbf{j}^+ \rangle_{\Gamma^-} - \mathrm{i}\langle \lambda^-, \mathbf{e}^+ \rangle_{\Gamma^-} + \langle \lambda^-, \mathbf{f}^{\mathrm{inc}} \rangle_{\Gamma^-} \tag{4.12}$$

$$\langle \beta^+, \mathbf{j}^+ \rangle_{\Gamma^+} - \mathrm{i}\langle \beta^+, \mathbf{e}^+ \rangle_{\Gamma^+} = -\langle \beta^+, \mathbf{j}^- \rangle_{\Gamma^+} - \mathrm{i}\langle \beta^+, \mathbf{e}^- \rangle_{\Gamma^+} - \langle \beta^+, \mathbf{g}^{\mathrm{inc}} \rangle_{\Gamma^+} \tag{4.13}$$

$$\langle \lambda^+, \mathbf{j}^+ \rangle_{\Gamma^+} - \mathrm{i}\langle \lambda^+, \mathbf{e}^+ \rangle_{\Gamma^+} = -\langle \lambda^+, \mathbf{j}^- \rangle_{\Gamma^+} - \mathrm{i}\langle \lambda^+, \mathbf{e}^- \rangle_{\Gamma^+} - \langle \lambda^+, \mathbf{g}^{\mathrm{inc}} \rangle_{\Gamma^+} \tag{4.14}$$

$$\forall \beta^{\pm} \in \mathbf{H}_{\perp}^{-1/2}(\mathrm{curl}_{\Gamma}; \Gamma^{\pm}) \text{ and } \lambda^{\pm} \in \mathbf{H}^{-1/2}(\mathrm{div}_{\Gamma}; \Gamma^{\pm})$$

Substituting (4.8) into (4.13) and (4.7) into (4.14) results in

$$\begin{aligned} &\frac{1}{2}\langle \beta^+, \mathbf{j}^+ \rangle_{\Gamma^+} + \langle \beta^+, \mathscr{S}_k(\mathbf{e}^+ \times \mathbf{n}) \rangle_{\Gamma^+} - \langle \beta^+, \mathscr{C}_k(\mathbf{j}^+) \rangle_{\Gamma^+} - \mathrm{i}\langle \beta^+, \mathbf{e}^+ \rangle_{\Gamma^+} \\ &\quad = -\langle \beta^+, \mathbf{j}^- \rangle_{\Gamma^+} - \mathrm{i}\langle \beta^+, \mathbf{e}^- \rangle_{\Gamma^+} - \langle \beta^+, \mathbf{g}^{\mathrm{inc}} \rangle_{\Gamma^+} \end{aligned} \tag{4.15}$$

$$\begin{aligned} &\langle \lambda^+, \mathbf{j}^+ \rangle_{\Gamma^+} - \frac{\mathrm{i}}{2}\langle \lambda^+, \mathbf{e}^+ \rangle_{\Gamma^+} + \mathrm{i}\langle \lambda^+, \mathscr{B}_k(\mathbf{e}^+ \times \mathbf{n}) \rangle_{\Gamma^+} - \mathrm{i}\langle \lambda^+, \mathscr{N}_k(\mathbf{j}^+) \rangle_{\Gamma^+} \\ &\quad = -\langle \lambda^+, \mathbf{j}^- \rangle_{\Gamma^+} - \mathrm{i}\langle \lambda^+, \mathbf{e}^- \rangle_{\Gamma^+} - \langle \lambda^+, \mathbf{g}^{\mathrm{inc}} \rangle_{\Gamma^+} \end{aligned} \tag{4.16}$$

We remark here the use of the Robin-type transmission conditions is in essence applying the combined-field integral equation (CFIE) for the boundary elements. This remark will be more evident once the final variational formulation for the coupled system is presented.

The finite-dimensional version of the variational formulation can be stated as

Seek $\mathbf{e}_h^{\pm} \in \mathscr{V}_h^{\pm}$ and $\mathbf{j}_h^{\pm} \in \mathscr{W}_h^{\pm}$ such that

$$\langle \beta_h^-, \mathbf{j}_h^- \rangle_{\mathscr{D}_h^-} - \mathrm{i}\langle \beta_h^-, \mathbf{e}_h^- \rangle_{\mathscr{D}_h^-} = -\langle \beta_h^-, \mathbf{j}_h^+ \rangle_{\mathscr{D}_h^-} - \mathrm{i}\langle \beta_h^-, \mathbf{e}_h^+ \rangle_{\mathscr{D}_h^-} + \langle \beta_h^-, \mathbf{f}^{\mathrm{inc}} \rangle_{\mathscr{D}_h^-}$$

$$\langle \lambda_h^-, \mathbf{j}_h^- \rangle_{\mathscr{D}_h^-} - \mathrm{i}\langle \lambda_h^-, \mathbf{e}_h^- \rangle_{\mathscr{D}_h^-} = -\langle \lambda_h^-, \mathbf{j}_h^+ \rangle_{\mathscr{D}_h^-} - \mathrm{i}\langle \lambda_h^-, \mathbf{e}_h^+ \rangle_{\mathscr{D}_h^-} + \langle \lambda_h^-, \mathbf{f}^{\mathrm{inc}} \rangle_{\mathscr{D}_h^-}$$

$$\begin{aligned} &\frac{1}{2}\langle \beta_h^+, \mathbf{j}_h^+ \rangle_{\mathscr{D}_h^+} + \langle \beta_h^+, \mathscr{S}_k(\mathbf{e}_h^+ \times \mathbf{n}) \rangle_{\mathscr{D}_h^+} - \langle \beta_h^+, \mathscr{C}_k(\mathbf{j}_h^+) \rangle_{\mathscr{D}_h^+} - \mathrm{i}\langle \beta_h^+, \mathbf{e}_h^+ \rangle_{\mathscr{D}_h^+} \\ &\quad = -\langle \beta_h^+, \mathbf{j}_h^- \rangle_{\mathscr{D}_h^+} - \mathrm{i}\langle \beta_h^+, \mathbf{e}_h^- \rangle_{\mathscr{D}_h^+} - \langle \beta_h^+, \mathbf{g}^{\mathrm{inc}} \rangle_{\mathscr{D}_h^+} \langle \lambda_h^+, \mathbf{j}_h^+ \rangle_{\mathscr{D}_h^+} - \frac{\mathrm{i}}{2}\langle \lambda_h^+, \mathbf{e}_h^+ \rangle_{\mathscr{D}_h^+} \\ &\qquad + \mathrm{i}\langle \lambda_h^+, \mathscr{B}_k(\mathbf{e}_h^+ \times \mathbf{n}) \rangle_{\mathscr{D}_h^+} - \mathrm{i}h\langle \lambda_h^+, \mathscr{N}_k(\mathbf{j}_h^+) \rangle_{\mathscr{D}_h^+} = -\langle \lambda_h^+, \mathbf{j}_h^- \rangle_{\mathscr{D}_h^+} - \mathrm{i}\langle \lambda_h^+, \mathbf{e}_h^- \rangle_{\mathscr{D}_h^+} \\ &\qquad - \langle \lambda_h^+, \mathbf{g}^{\mathrm{inc}} \rangle_{\mathscr{D}_h^+} \quad \forall \beta_h^{\pm} \in \mathscr{V}_h^{\pm} \text{ and } \lambda_h^{\pm} \in \mathscr{W}_h^{\pm} \end{aligned} \tag{4.17}$$

4.5. The final variational formulation for symmetric FEM–BEM couplings

The final variational formulation for the couplings between FEMs and BEMs is accomplished by substituting the first equation of (4.17) into the interior variational statement (4.5). Note that since $\gamma_t^- \mathbf{v}_h \in \mathscr{V}_h^-$ in (4.5), according to the first equation of (4.17), we have

$$\langle \gamma_t^- \mathbf{v}_h, \mathbf{j}_h^- \rangle_{\mathscr{D}_h^-} = \mathrm{i}\langle \gamma_t^- \mathbf{v}_h, \mathbf{e}_h^- \rangle_{\mathscr{D}_h^-} - \langle \gamma_t^- \mathbf{v}_h, \mathbf{j}_h^+ \rangle_{\mathscr{D}_h^-} - \mathrm{i}\langle \gamma_t^- \mathbf{v}_h, \mathbf{e}_h^+ \rangle_{\mathscr{D}_h^-} + \langle \gamma_t^- \mathbf{v}_h, \mathbf{f}^{\mathrm{inc}} \rangle_{\mathscr{D}_h^-} \tag{4.18}$$

There is an additional trick for the symmetric couplings in the current formulation. That is we split the boundary integral term in (4.5), $\langle \gamma_t^- \mathbf{v}_h, \mathbf{j}_h^- \rangle_{\mathscr{D}_h^-}$, into two halves and only substituting (4.18) for one of the two halves. Thus, we rewrite (4.5) as

Given $\mathbf{j}_h^- \in \mathscr{W}_h^-$, seek $\mathbf{E}_h \in \mathscr{X}_h$ such that

$$\mathscr{A}(\mathbf{v}_h,\mathbf{E}_h)_{\Omega_h} - \frac{k}{2}\langle \gamma_t^- \mathbf{v}_h, \mathbf{j}_h^- \rangle_{\mathscr{D}_h^-} - \frac{ik}{2}\langle \gamma_t^- \mathbf{v}_h, \mathbf{e}_h^- \rangle_{\mathscr{D}_h^-} + \frac{k}{2}\langle \gamma_t^- \mathbf{v}_h, \mathbf{j}_h^+ \rangle_{\mathscr{D}_h^-} + \frac{ik}{2}\langle \gamma_t^- \mathbf{v}_h, \mathbf{e}_h^+ \rangle_{\mathscr{D}_h^-} = \frac{k}{2}\langle \gamma_t^- \mathbf{v}_h, \mathbf{f}^{\text{inc}} \rangle_{\mathscr{D}_h^-} \quad \forall \mathbf{v}_h \in \mathscr{X}_h \tag{4.19}$$

To complete the formulation for the couplings between FEMs and BEMs, we add the last three equations of (4.17)–(4.19) and write

Seek $\mathbf{E}_h \in \mathscr{X}_h, \mathbf{e}_h^+ \in \mathscr{V}_h^+$ and $\mathbf{j}_h^\pm \in \mathscr{W}_h^\pm$ such that

$$\begin{aligned}
&\mathscr{A}(\mathbf{v}_h,\mathbf{E}_h)_{\Omega_h} - \frac{ik}{2}\langle \gamma_t^- \mathbf{v}_h, \gamma_t^- \mathbf{E}_h \rangle_{\mathscr{D}_h^-} - \frac{k}{2}\langle \gamma_t^- \mathbf{v}_h, \mathbf{j}_h^- \rangle_{\mathscr{D}_h^-} + \frac{ik}{2}\langle \gamma_t^- \mathbf{v}_h, \mathbf{e}_h^+ \rangle_{\mathscr{D}_h^-} + \frac{k}{2}\langle \gamma_t^- \mathbf{v}_h, \mathbf{j}_h^+ \rangle_{\mathscr{D}_h^-} \\
&\quad = \frac{k}{2}\langle \gamma_t^- \mathbf{v}_h, \mathbf{f}^{\text{inc}} \rangle_{\mathscr{D}_h^-} \\
&\frac{k}{2}\langle \lambda_h^-, \gamma_t^- \mathbf{E}_h \rangle_{\mathscr{D}_h^-} + \frac{ik}{2}\langle \lambda_h^-, \mathbf{j}_h^- \rangle_{\mathscr{D}_h^-} - \frac{k}{2}\langle \lambda_h^-, \mathbf{e}_h^+ \rangle_{\mathscr{D}_h^-} + \frac{ik}{2}\langle \lambda_h^-, \mathbf{j}_h^+ \rangle_{\mathscr{D}_h^-} = \frac{ik}{2}\langle \lambda_h^-, \mathbf{f}^{\text{inc}} \rangle_{\mathscr{D}_h^-} \\
&\frac{ik}{2}\langle \beta_h^+, \gamma_t^- \mathbf{E}_h \rangle_{\mathscr{D}_h^+} + \frac{k}{2}\langle \beta_h^+, \mathbf{j}_h^- \rangle_{\mathscr{D}_h^+} + \frac{k}{2}\langle \beta_h^+, \mathscr{S}_k(\mathbf{e}_h^+ \times \mathbf{n}) - i\mathbf{e}_h^+ \rangle_{\mathscr{D}_h^+} \\
&\quad + \frac{k}{2}\left\langle \beta_h^+, \left(\frac{Id}{2} - \mathscr{C}_k\right)(\mathbf{j}_h^+) \right\rangle_{\mathscr{D}_h^+} = -\frac{k}{2}\langle \beta_h^+, \mathbf{g}^{\text{inc}} \rangle_{\mathscr{D}_h^+} \\
&-\frac{k}{2}\langle \lambda_h^+, \mathbf{e}_h^- \rangle_{\mathscr{D}_h^+} + \frac{ik}{2}\langle \lambda_h^+, \mathbf{j}_h^- \rangle_{\mathscr{D}_h^+} + \frac{k}{2}\left\langle \lambda_h^+, \frac{1}{2}\mathbf{e}_h^+ - \mathscr{B}_k(\mathbf{e}_h^+ \times \mathbf{n}) \right\rangle_{\mathscr{D}_h^+} \\
&\quad + \frac{ik}{2}\langle \lambda_h^+, (Id - i\mathscr{N}_k)(\mathbf{j}_h^+) \rangle_{\mathscr{D}_h^+} = -\frac{ik}{2}\langle \lambda_h^+, \mathbf{g}^{\text{inc}} \rangle_{\mathscr{D}_h^+} \quad \forall \mathbf{v}_h \in \mathscr{X}_h, \ \ \beta_h^+ \in \mathscr{V}_h^+ \text{ and } \forall \lambda_h^\pm \in \mathscr{W}_h^\pm
\end{aligned} \tag{4.20}$$

5. Matrix equation for the non-conformal symmetric couplings between finite and boundary elements

In the finite-dimensional discretization, we have employed the following approximations in tetrahedra and on triangles for the variables:

$\mathbf{E}_h$ second-order Nédélec elements of thefirst kind [23] in Ω_h
$\mathbf{j}_h^-$ second-order Raviart–Thomas elements [21] on $\mathscr{D}_h^-$
$\mathbf{e}_h^+$ edge elements on $\mathscr{D}_h^+$
$\mathbf{j}_h^+$ first-order Raviart–Thomas elements [21] on $\mathscr{D}_h^+$

Subsequently, the final matrix equation corresponding to the variational formulation (4.18) is of the form

$$\begin{bmatrix}
A_{II} & A_{I\Gamma} & 0 & 0 & 0 \\
A_{\Gamma I} & A_{\Gamma\Gamma} - \frac{ik}{2}T_{\Gamma^-\Gamma^-} & -\frac{k}{2}D_{\Gamma^-\Gamma^-} & \frac{ik}{2}T_{\Gamma^-\Gamma^+} & \frac{k}{2}D_{\Gamma^-\Gamma^+} \\
0 & \frac{k}{2}M_{\Gamma^-\Gamma^-} & \frac{ik}{2}T_{\Gamma^-\Gamma^-} & -\frac{k}{2}M_{\Gamma^-\Gamma^+} & \frac{ik}{2}T_{\Gamma^-\Gamma^+} \\
0 & \frac{ik}{2}T_{\Gamma^+\Gamma^-} & \frac{k}{2}D_{\Gamma^+\Gamma^-} & \frac{k}{2}Q_e - \frac{ik}{2}T_{\Gamma^+\Gamma^+} & \frac{k}{2}P \\
0 & -\frac{k}{2}M_{\Gamma^+\Gamma^-} & \frac{ik}{2}T_{\Gamma^+\Gamma^-} & \frac{k}{2}U & \frac{k}{2}Q_j + \frac{ik}{2}T_{\Gamma^+\Gamma^+}
\end{bmatrix}
\begin{bmatrix}
\mathbf{E}_h^{\text{int}} \\ \mathbf{e}_h^- \\ \mathbf{j}_h^- \\ \mathbf{e}_h^+ \\ \mathbf{j}_h^+
\end{bmatrix}
= \begin{bmatrix} 0 & \frac{k}{2}\mathbf{f}_e^{\text{inc}} & \frac{ik}{2}\mathbf{f}_j^{\text{inc}} & -\frac{k}{2}\mathbf{g}_e^{\text{inc}} & -\frac{ik}{2}\mathbf{g}_j^{\text{inc}} \end{bmatrix}^t \tag{5.1}$$

Note that in Eq. (5.1), we have partitioned the unknown coefficients of $\mathbf{E}_h$ into $\mathbf{E}_h^{\text{int}}$ and $\mathbf{e}_h^-$ for the interior and surface unknowns, respectively. The sub-matrices and their corresponding bilinear forms are summarized below:

$$\begin{bmatrix} A_{II} & A_{I\Gamma} \\ A_{\Gamma I} & A_{\Gamma\Gamma} \end{bmatrix} : \mathscr{A}(\mathbf{v},\mathbf{E}), \quad T_{\Gamma^-\Gamma^-} : \langle \gamma_t^- \mathbf{v}_h, \mathbf{e}_h^- \rangle_{\mathscr{D}_h^-}, \quad T_{\Gamma^+\Gamma^+} : \langle \beta_h^+, \mathbf{e}_h^+ \rangle_{\mathscr{D}_h^+}, \quad T_{\Gamma^-\Gamma^+} : \langle \gamma_t^- \mathbf{v}_h, \mathbf{e}_h^+ \rangle_{\mathscr{D}_h^-},$$
$$T_{\Gamma^+\Gamma^-} : \langle \beta_h^+, \mathbf{e}_h^- \rangle_{\mathscr{D}_h^+}, \quad D_{\Gamma^-\Gamma^-} : \langle \gamma_t^- \mathbf{v}_h, \mathbf{j}_h^- \rangle_{\mathscr{D}_h^-}, \quad D_{\Gamma^-\Gamma^+} : \langle \gamma_t^- \mathbf{v}_h, \mathbf{j}_h^+ \rangle_{\mathscr{D}_h^-}, \quad D_{\Gamma^+\Gamma^-} : \langle \beta_h^+, \mathbf{j}_h^- \rangle_{\mathscr{D}_h^+},$$
$$M_{\Gamma^-\Gamma^-} : \langle \lambda_h^-, \mathbf{e}_h^- \rangle_{\mathscr{D}_h^-}, \quad M_{\Gamma^+\Gamma^-} : \langle \lambda_h^+, \mathbf{e}_h^- \rangle_{\mathscr{D}_h^+}, \quad Q_e : \langle \beta_h^+, \mathscr{S}_k(\mathbf{e}_h^+ \times \mathbf{n}) \rangle_{\mathscr{D}_h^+}, \quad Q_j : \langle \lambda_h^+, \mathscr{N}_k(\mathbf{j}_h^+) \rangle_{\mathscr{D}_h^+},$$
$$P : \left\langle \beta_h^+, (\frac{1}{2}\mathscr{I} - \mathscr{C}_k)(\mathbf{j}_h^+) \right\rangle_{\mathscr{D}_h^+}, \quad U : \left\langle \lambda_h^+, \frac{1}{2}\mathbf{e}_h^+ - \mathscr{B}_k(\mathbf{e}_h^+ \times \mathbf{n}) \right\rangle_{\mathscr{D}_h^+} \tag{5.2}$$

Moreover, the right-hand side of (5.1) corresponds to

$$\mathbf{f}_e^{\text{inc}} := \langle \gamma_t^- \mathbf{v}_h, \mathbf{f}^{\text{inc}} \rangle_{\mathscr{D}_h^-}, \quad \mathbf{f}_j^{\text{inc}} := \langle \lambda_h^-, \mathbf{f}^{\text{inc}} \rangle_{\mathscr{D}_h^-}$$
$$\mathbf{g}_e^{\text{inc}} := \langle \beta_h^+ \mathbf{g}^{\text{inc}} \rangle_{\mathscr{D}_h^+}, \quad \mathbf{g}_j^{\text{inc}} := \langle \lambda_h^+, \mathbf{g}^{\text{inc}} \rangle_{\mathscr{D}_h^+} \tag{5.3}$$

The symmetry of the matrix in (5.1) can be established by noting the following symmetries:

$$\langle \beta_i, \beta_j \times \mathbf{n} \rangle_{\mathscr{D}} = -\langle \beta_i \times \mathbf{n}, \beta_j \rangle_{\mathscr{D}}; \quad \langle \beta_i, \mathscr{C}_k(\beta_j \times \mathbf{n}) \rangle_{\mathscr{D}} = -\langle \beta_j, \mathscr{C}_k(\beta_i \times \mathbf{n}) \rangle_{\mathscr{D}}$$
$$\langle \beta_i, \mathscr{S}_k(\beta_j \times \mathbf{n}) \rangle_{\mathscr{D}} = \langle \beta_j, \mathscr{S}_k(\beta_i \times \mathbf{n}) \rangle_{\mathscr{D}}; \quad \langle \lambda_i, \mathscr{N}_k(\lambda_j) \rangle_{\mathscr{D}} = \langle \lambda_j, \mathscr{N}_k(\lambda_i) \rangle_{\mathscr{D}} \tag{5.4}$$

where β_i is the ith basis function in $\mathscr{V}_h^{\pm}$, λ_i the ith basis function in $\mathscr{W}_h^{\pm}$ and the surface triangulation $\mathscr{D}$ can be either $\mathscr{D}_h^-$ or $\mathscr{D}_h^+$. Then it follows directly:

$$M_{\Gamma^-\Gamma^-} = -D_{\Gamma^-\Gamma^-}^t, \quad M_{\Gamma^-\Gamma^+} = -D_{\Gamma^+\Gamma^-}^t, \quad T_{\Gamma^+\Gamma^-} = T_{\Gamma^-\Gamma^+}^t$$
$$U = -P = P^t, \quad Q_e = Q_e^t, \quad Q_j = Q_j^t \tag{5.5}$$

6. Physical interpretation of FEM–BEM couplings using domain decomposition approach

6.1. Simple description of the DD–FE–BE process

Although in practical applications, the boundary Γ, which separates the interior FEM region Ω and the exterior IE region Ω^c tends to be conformal to the problem geometry and can be arbitrary, we shall gain significant physical insight without altering much of the problem nature by considering Γ a sphere enclosing all the scatterers inside. Referring to Fig. 2, in the first iteration of the DD–FE–BE process, we simply solve the interior FEM problem with a classical first-order Absorbing Boundary Condition (ABC) employed on the truncation boundary Γ. Hence, the solution, as depicted in Fig. 2, consists of three fields: the incident field ($\mathbf{E}_{\text{i}}^{(1)} (\equiv \mathbf{E}^{\text{inc}})$), the scattered field ($\mathbf{E}_{\text{s}}^{(1)}$) from the scatterers and the reflected field ($\mathbf{E}_{\text{R}}^{(1)}$) due to the truncation boundary Γ. However, since the reflected field, $\mathbf{E}_{\text{R}}^{(1)}$, does not provide legitimate Cauchy data for the exterior region Ω^c and therefore does not satisfy the exterior Calderon projector in (3.9). This reflected field, $\mathbf{E}_{\text{R}}^{(1)}$, becomes the source for the next domain decomposition iteration as shown in Fig. 2(c). Namely, we

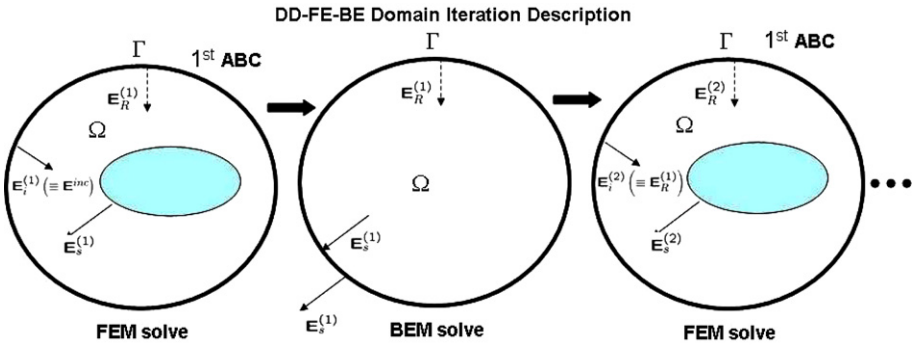

Fig. 2. A simple physical interpretation of the DD–FE–BE iteration process.

have $\mathbf{E}_{\mathrm{i}}^{(2)} = \mathbf{E}_{\mathrm{R}}^{(1)}$. Once again, the "new" incident field will produce a FEM solution in Ω, which consists of the incident wave, $\mathbf{E}_{\mathrm{i}}^{(2)}$, the scattered field, $\mathbf{E}_{\mathrm{s}}^{(2)}$ and the reflected field, $\mathbf{E}_{\mathrm{R}}^{(2)}$. This process continues until we exhaust the maximum number of DD iterations or the DD process converged with $\|\mathbf{E}_{\mathrm{i}}^{n}\| < \delta\|\mathbf{E}_{\mathrm{i}}^{0}\|$, δ a prescribed tolerance.

From the physical picture just painted, it is clear that for the DD process to converge, we need to ascertain that

$$\frac{\|\mathbf{E}_{\mathrm{R}}^{(i)}\|}{\|\mathbf{E}_{\mathrm{s}}^{(i)}\|} < 1 \tag{6.1}$$

Mathematically, Eq. (6.1) is the same as requiring that

$$\rho\begin{pmatrix} 0 & \mathscr{A}_{\mathrm{FEM}}^{-1}\mathscr{A}_{\mathrm{C}} \\ \mathscr{A}_{\mathrm{BEM}}^{-1}\mathscr{A}_{\mathrm{C}}^{t} & 0 \end{pmatrix} < 1 \tag{6.2}$$

in order to assure a converging DD–FE–BE iterative process. Note that the sub-matrices $\mathscr{A}_{\mathrm{FEM}}$ and $\mathscr{A}_{\mathrm{BEM}}$ are denoted for the matrices corresponding to FEM and BEM unknowns respectively and the sub-matrix $\mathscr{A}_{\mathrm{C}}$ denotes the coupling matrix between the FEM and BEM variables.

We shall prove next that (6.1) indeed holds for Γ a sphere. Afterward, we take a leap of faith and hypothesize that (6.1) holds true even for non-sphere boundary Γ so long as it is convex. Numerical results presented later in this paper support this assertion, though we do not have concrete proof of such claim.

6.2. Reflection of spherical harmonics at a spherical boundary

As discussed in [24], due to the orthogonality of the harmonics, to study the reflection of fields at a spherical boundary, we only need to consider one harmonic at a time. Moreover, the TM and TE waves are also decoupled. Hence, we start by expressing the scattered fields of the TM modes, the transverse components, inside the sphere as

$$\begin{aligned} \begin{bmatrix} E_\theta^{\mathrm{s}} \\ E_\phi^{\mathrm{s}} \end{bmatrix} &= \frac{\mathrm{i}\eta}{k}\begin{bmatrix} \frac{\partial}{\partial\theta}P_n^m(\cos\theta) \\ \frac{\mathrm{i}m}{\sin\theta}P_n^m(\cos\theta) \end{bmatrix}\frac{1}{r}\frac{\partial}{\partial r}\left(rh_n^{(1)}(kr)\right) \\ \begin{bmatrix} H_\theta^{\mathrm{s}} \\ H_\phi^{\mathrm{s}} \end{bmatrix} &= \frac{\mathrm{i}\eta}{k}\begin{bmatrix} \frac{\mathrm{i}m}{\sin\theta}P_n^m(\cos\theta) \\ -\frac{\partial}{\partial\theta}P_n^m(\cos\theta) \end{bmatrix}h_n^{(1)}(kr) \end{aligned} \tag{6.3}$$

where h_n^1 is the first kind of Hankel function with index n. Similarly, the reflected fields are written as

$$\begin{aligned} \begin{bmatrix} E_\theta^{\mathrm{R}} \\ E_\phi^{\mathrm{R}} \end{bmatrix} &= \frac{\mathrm{i}R_{\mathrm{TM}}\eta}{k}\begin{bmatrix} \frac{\partial}{\partial\theta}P_n^m(\cos\theta) \\ \frac{\mathrm{i}m}{\sin\theta}P_n^m(\cos\theta) \end{bmatrix}\frac{1}{r}\frac{\partial}{\partial r}\left(rh_n^{(2)}(kr)\right) \\ \begin{bmatrix} H_\theta^{\mathrm{s}} \\ H_\phi^{\mathrm{s}} \end{bmatrix} &= \frac{\mathrm{i}R_{\mathrm{TM}}\eta}{k}\begin{bmatrix} \frac{\mathrm{i}m}{\sin\theta}P_n^m(\cos\theta) \\ -\frac{\partial}{\partial\theta}P_n^m(\cos\theta) \end{bmatrix}h_n^{(2)}(kr) \end{aligned} \tag{6.4}$$

and $h_n^{(2)}$ is the second kind of Hankel functions. Note that the cement variables are related to the magnetic fields through $\mathbf{J} = -\mathrm{i}\eta\mathbf{H}\times\hat{r}$. Substituting (6.3) and (6.4) into the first-order ABC at $r = a$ results in

$$-h_n^{(1)}(ka) - R_{\mathrm{TM}}h_n^{(2)} - \mathrm{i}\left\{\frac{1}{ka}\left(h_n^{(1)}(ka) + kah_n^{(1)'}(ka)\right) + \frac{R_{\mathrm{TM}}}{ka}\left(h_n^{(2)}(ka) + kah_n^{(2)'}(ka)\right)\right\} = 0 \tag{6.5}$$

Eq. (6.5) gives an expression for the reflection coefficient R_{TM}:

$$R_{\mathrm{TM}} = -\frac{kah_n^{(1)}(ka) - \mathrm{i}h_n^{(1)} - \mathrm{i}kah_n^{(1)'}(ka)}{kah_n^{(2)}(ka) + \mathrm{i}h_n^{(2)}(ka) + \mathrm{i}kah_n^{(2)'}(ka)} \tag{6.6}$$

Note that R_{TM} only depends on n and is independent of m. A similar expression for R_{TE} can be obtained as well and it is

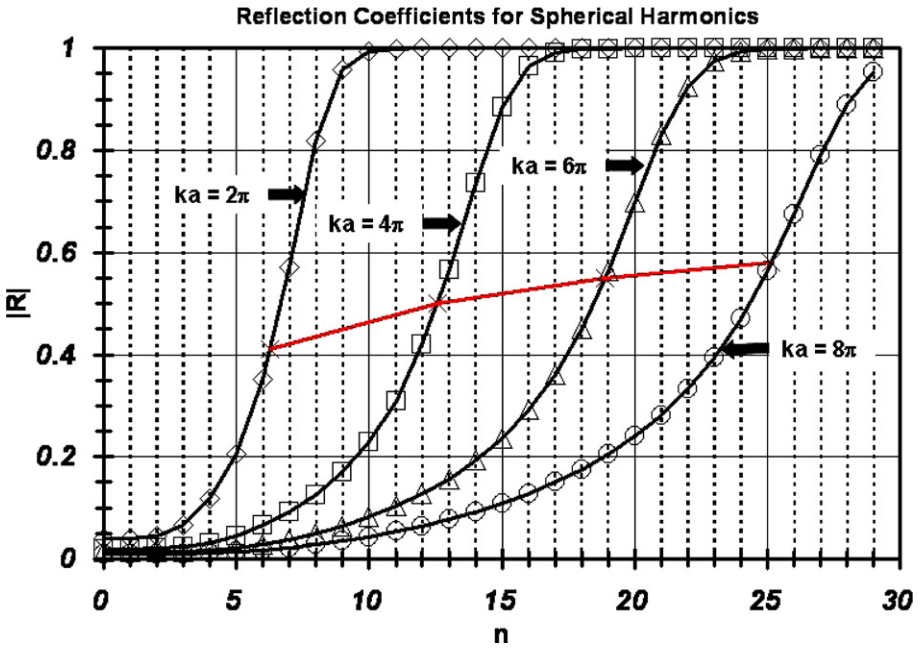

Fig. 3. The reflection coefficients of spherical harmonics at spherical boundary for different values of ka.

$$R_{\mathrm{TE}} = \frac{\mathrm{i}kah_n^{(1)}(ka) - h_n^{(1)} - kah_n^{(1)'}(ka)}{h_n^{(2)}(ka) - \mathrm{i}kah_n^{(2)}(ka) + kah_n^{(2)'}(ka)} \tag{6.7}$$

We note here that the magnitudes of R_{TE} and R_{TM} are the same for same value of the harmonic index n. We plot the magnitude of the reflection as a function of the harmonic index n for different ka values in Fig. 3. Also, in Fig. 3, we connect the points, with $n = ka$, on different curves to form a trendline (the solid line with crosses on). From Fig. 3, we make the following observations concerning the convergence in the DD–FE–BE process:

1. For a physical problem with a fixed operating frequency, we can improve the convergence in the DD–FE–BE process significantly by increasing the radius, a, of the boundary Γ. This, however, does come at the expense of taxing more computational resources since the number of unknowns in the FEM and BEM portion will no doubt scale by $\mathrm{O}(a^3)$ and $\mathrm{O}(a^2)$, respectively;
2. Plotted in Fig. 3 is a sample trendline which connects $|R|$ at $n = ka$ for different ka values (the curve with crosses on). Since that for a given physical problem, the maximum harmonic index $n_{\max}$ is proportional to ka, thus, the trendline indicates the convergence performance of the DD–FE–BE process as the frequency increases. As shown in the figure, the couplings between FEMs and BEMs do increase (namely the largest effective reflection coefficients), however, only slightly. This suggests that the proposed DD–FE–BE formulation should be relatively robust for modeling electrically large problems.

7. Preconditioner and iterative matrix solution

There are three preconditioners that we used in this study. They are: a domain diagonal block (DDB) preconditioner; an Additive-Multiplicative Schwarz (AMS) preconditioner; and a Multiplicative-Multiplicative Schwarz (MMS) preconditioner. To describe these three preconditioning strategies in full, we first partition the matrix in (5.1) into

$$\mathscr{A} = \begin{bmatrix} \mathscr{A}_{\mathrm{FEM}} & \mathscr{A}_{\mathrm{C}} \\ \mathscr{A}_{\mathrm{C}}^t & \mathscr{A}_{\mathrm{BEM}} \end{bmatrix} \tag{7.1}$$

where $\mathscr{A}_{\mathrm{FEM}}$ and $\mathscr{A}_{\mathrm{BEM}}$ are the matrix blocks correspond to finite element unknowns ($\mathbf{E}_h^{\mathrm{int}}$, $\mathbf{e}_h^-$ and $\mathbf{j}_h^-$) and triangular boundary elements ($\mathbf{e}_h^+$ and $\mathbf{j}_h^+$), respectively. Naturally, $\mathscr{A}_{\mathrm{C}}$ represents the couplings between FEMs and BEMs.

The three preconditioning strategies that we used in this study are all based on preconditioners for A_{FEM} and A_{BEM}. Hence, we shall elaborate their constructions in detail first. Denote the preconditioners for $\mathscr{A}_{\mathrm{FEM}}$ and $\mathscr{A}_{\mathrm{BEM}}$ as $\overline{\mathscr{M}}_{\mathrm{FEM}}$ and $\overline{\mathscr{M}}_{\mathrm{BEM}}$, respectively. Since we are using $p = 2$ hierarchical Nédélec mixed $\mathbf{H}(\mathrm{curl})$ elements for $\mathbf{E}_h$ and $p = 2$ hierarchical Raviart–Thomas $\mathbf{H}(\mathrm{div})$ elements on triangles for $\mathbf{j}_h^-$, the FEM matrix block can be further partitioned into

$$\mathscr{A}_{\mathrm{FEM}} = \begin{bmatrix} \mathscr{A}_{1,1} & \mathscr{A}_{1,2} \\ \mathscr{A}_{2,1} & \mathscr{A}_{2,2} \end{bmatrix} \tag{7.2}$$

where $\mathscr{A}_{1,1}$ and $\mathscr{A}_{2,2}$ represent the first- and the second-order basis functions blocks, respectively. Obviously, $\mathscr{A}_{1,2}$ and $\mathscr{A}_{2,1}$ are the couplings between the first- and the second-order finite elements. Borrowing the pMUS preconditioner developed in [25,26], the preconditioner $\overline{\mathscr{M}}_{\mathrm{FEM}}$ is constructed as

$$\overline{\mathscr{M}}_{\mathrm{FEM}} = \begin{bmatrix} \mathscr{I} & -\left(\mathscr{C}_{1,1}^t \mathscr{C}_{1,1}\right)^{-1} \mathscr{A}_{1,2} \\ 0 & \mathscr{I} \end{bmatrix} \begin{bmatrix} \left(\mathscr{C}_{1,1}^t \mathscr{C}_{1,1}\right)^{-1} & 0 \\ 0 & \left(\mathscr{C}_{2,2}^t \mathscr{C}_{2,2}\right)^{-1} \end{bmatrix} \begin{bmatrix} \mathscr{I} & 0 \\ -\mathscr{A}_{2,1}\left(\mathscr{C}_{1,1}^t \mathscr{C}_{1,1}\right)^{-1} & \mathscr{I} \end{bmatrix} \tag{7.3}$$

where we have set $\mathscr{C}_{1,1}^t \mathscr{C}_{1,1} = \mathrm{ICD}(\mathscr{A}_{1,1}, 10^{-6})$ and $\mathscr{C}_{2,2}^t \mathscr{C}_{2,2} = \mathrm{ICD}(\mathscr{A}_{2,2}, 10^{-3})$; $\mathrm{ICD}(\mathscr{A}, \epsilon)$ denotes the incomplete Choleski factorization of matrix $\mathscr{A}$ with drop tolerance of ϵ. We should remark here that the effectiveness of the pMUS preconditioner depends strongly on the couplings between different polynomial orders of basis function groups. The weaker that they are coupled, the more effective the pMUS preconditioner will be. On the detailed construction of nearly orthogonal hierarchical Nédélec mixed elements, we refer to Ref. [25].

The construction of the $\overline{\mathscr{M}}_{\mathrm{BEM}}$ involves first a sparse version of the $\mathscr{A}_{\mathrm{BEM}}$, namely $\mathscr{Z}_{\mathrm{BEM}}$. The sparse matrix $\mathscr{Z}_{\mathrm{BEM}}$ is constructed through the same procedure as described in [10], subsequently, we obtain the preconditioner $\overline{\mathscr{M}}_{\mathrm{BEM}}$ simply by $\overline{\mathscr{M}}_{\mathrm{BEM}} = \mathrm{ICD}(\mathscr{Z}_{\mathrm{BEM}}, 0.0)$.

7.1. Domain diagonal block (DDB) preconditioner with inner–outer loop iterations

Domain decomposition method [27] can often be viewed as a preconditioner for Krylov subspace solver such as Conjugate Gradient (CG) method. The simplest and the most natural DD method based preconditioner is the additive Schwarz preconditioner. This is equivalent to a diagonal block preconditioner, where the preconditioner M_{DDB} has the form

$$\mathscr{M}_{\mathrm{DDB}}^{-1} = \begin{bmatrix} \mathscr{A}_{\mathrm{FEM}}^{-1} & 0 \\ 0 & \mathscr{A}_{\mathrm{BEM}}^{-1} \end{bmatrix} \tag{7.4}$$

However, instead of direct factorizations of $\mathscr{A}_{\mathrm{FEM}}$ and $\mathscr{A}_{\mathrm{BEM}}$, which are costly operations, we perform inner loop iterative matrix solutions. Namely, for each outer CG iteration for (5.1), we shall solve for $\mathscr{A}_{\mathrm{FEM}} z_{\mathrm{FEM}} = r_{\mathrm{FEM}}$ and $\mathscr{A}_{\mathrm{BEM}} z_{\mathrm{BEM}} = r_{\mathrm{BEM}}$, again using preconditioned CG method. We have used relative residuals of 10^{-6} for the inner loop iterations for both FEM and BEM matrix equations.

7.2. Additive–multiplicative Schwarz (AMS) preconditioner

With the availability of $\overline{\mathscr{M}}_{\mathrm{FEM}}$ and $\overline{\mathscr{M}}_{\mathrm{BEM}}$, the AMS preconditioner, $\mathscr{M}_{\mathrm{AMS}}$, for the DD–FE–BEM matrix can be simply computed by

$$\mathscr{M}_{\mathrm{AMS}}^{-1} = \begin{bmatrix} \overline{\mathscr{M}}_{\mathrm{FEM}}^{-1} & 0 \\ 0 & \overline{\mathscr{M}}_{\mathrm{BEM}}^{-1} \end{bmatrix} \tag{7.5}$$

7.3. Multiplicative–multiplicative Schwarz (MMS) preconditioner

The multiplicative–multiplicative Schwarz (MMS) preconditioner, $\mathscr{M}_{\mathrm{MMS}}$, is constructed by recognizing the weak couplings between finite and boundary elements. Applying the multiplicative Schwarz method again to (7.1) results in

$$\mathscr{M}_{\mathrm{MMS}} = \begin{bmatrix} \mathscr{I} & -\overline{\mathscr{M}}^{-1}_{\mathrm{FEM}}\mathscr{A}_{\mathrm{C}} \\ 0 & \mathscr{I} \end{bmatrix} \begin{bmatrix} \overline{\mathscr{M}}^{-1}_{\mathrm{FEM}} & 0 \\ 0 & \overline{\mathscr{M}}^{-1}_{\mathrm{BEM}} \end{bmatrix} \begin{bmatrix} \mathscr{I} & 0 \\ -\mathscr{A}^{t}_{\mathrm{C}}\overline{\mathscr{M}}^{-1}_{\mathrm{FEM}} & \mathscr{I} \end{bmatrix} \tag{7.6}$$

8. Numerical results

For all the examples in this section, the FEM unknown space is spanned by the $p = 2$ Mixed Nédélec tetrahedral elements [23], while BEM utilizes $p = 1$ Raviart–Thomas elements [21] over a triangular support. Double precision arithmetic was used throughout the programs. The codes were designed in a completely modular object oriented fashion and the GNU g++ compiler with −O9 optimization level was used. All the computations, except for the cases explicitly stated otherwise, were performed on an AMD 64-bit Opteron 246 Workstation with 1024 KB L2 cache and 16 GB RAM.

8.1. Internal resonances and eigenspectrum study

Before start describing some real-life examples it is important to first verify some of the theoretical claims stated in the previous sections. First the internal resonance issue will be studied. A 1 m^2 box computational domain is first considered. The air box is discretized with approximately $h = \lambda_0/6$ tetrahedral elements, where λ_0 is the free space wavelength. For the present geometry the internal resonance (both TE and TM modes due to degeneracy) should occur around 212 MHz. To identify the presence or absence of internal resonances, an estimate spectral condition number $\kappa(\mathscr{A}) = \lambda_{\max}(\mathscr{A})/\lambda_{\min}(\mathscr{A})$ of the system matrix is computed in the neighborhood of the suspected resonance frequency. The condition number is estimated using the open source software SPARSE. The results are shown in Fig. 4(b) and (c) with solid blue line for the non-diagonal scaled and diagonal scaled matrices, respectively.[1] It is apparent that neither the diagonal scaled nor the non-diagonal scaled system shows signs of condition number increase around the resonance. On the other hand, the internal resonance problem surfaces exactly at 212 MHz when Costable's symmetric FEBI [6,9,10] is used. It is interesting that the diagonal scaling does affect the bandwidth of the resonance, but not the location of the resonance. Here it should be noted that the actual values in the condition number curves in subfigure (a) (Costabel's symmetric FEBI) versus (b) and (c) (proposed approach) should not be compared directly because the number of unknowns thus the size of the two matrices are different. To support the theory that the boundary integral formulation utilized here does not suffer forbidden frequencies, the BEM sub-matrix is plotted in black solid line. Notice that when the sparse matrix T is added (red solid line), the condition number improves (regularized) by one order.

To gain further insight on the numerical stability of the proposed formulation, the complete eigenvalue distribution of the coupling matrix, or more precisely the matrix $\mathscr{M}^{-1}_{\mathrm{DDB}}(\mathscr{A} - \mathscr{M}_{\mathrm{DDB}})$ is considered for the same one meter square box computational domain. The results are plotted in Fig. 5 for increasing mesh densities. It is observed most eigenvalues are inside the unity circle (propagating modes), only very few on the unit circle (evanescent modes, correspond to large values of harmonic index n in Eq. (6.6)), thus the spectral radius of the coupling matrix is less or equal to one. In many practical applications, the presence of evanescent modes is negligible and even if they are present they can be easily taken care by the Krylov iterations. However, in these situations, the use of the simple Gauss–Siedel iteration method may exhibit slow convergence or even diverge. Therefore, for robust matrix solution performance, we strongly recommend the use of Krylov subspace iteration methods. It is apparent that the spectrum has three accumulation centers: for low values of index n (propagating modes) around zero and large values of n (evanescent

[1] For interpretation of color in Figs. 4 and 6, the reader is referred to the web version of this article.

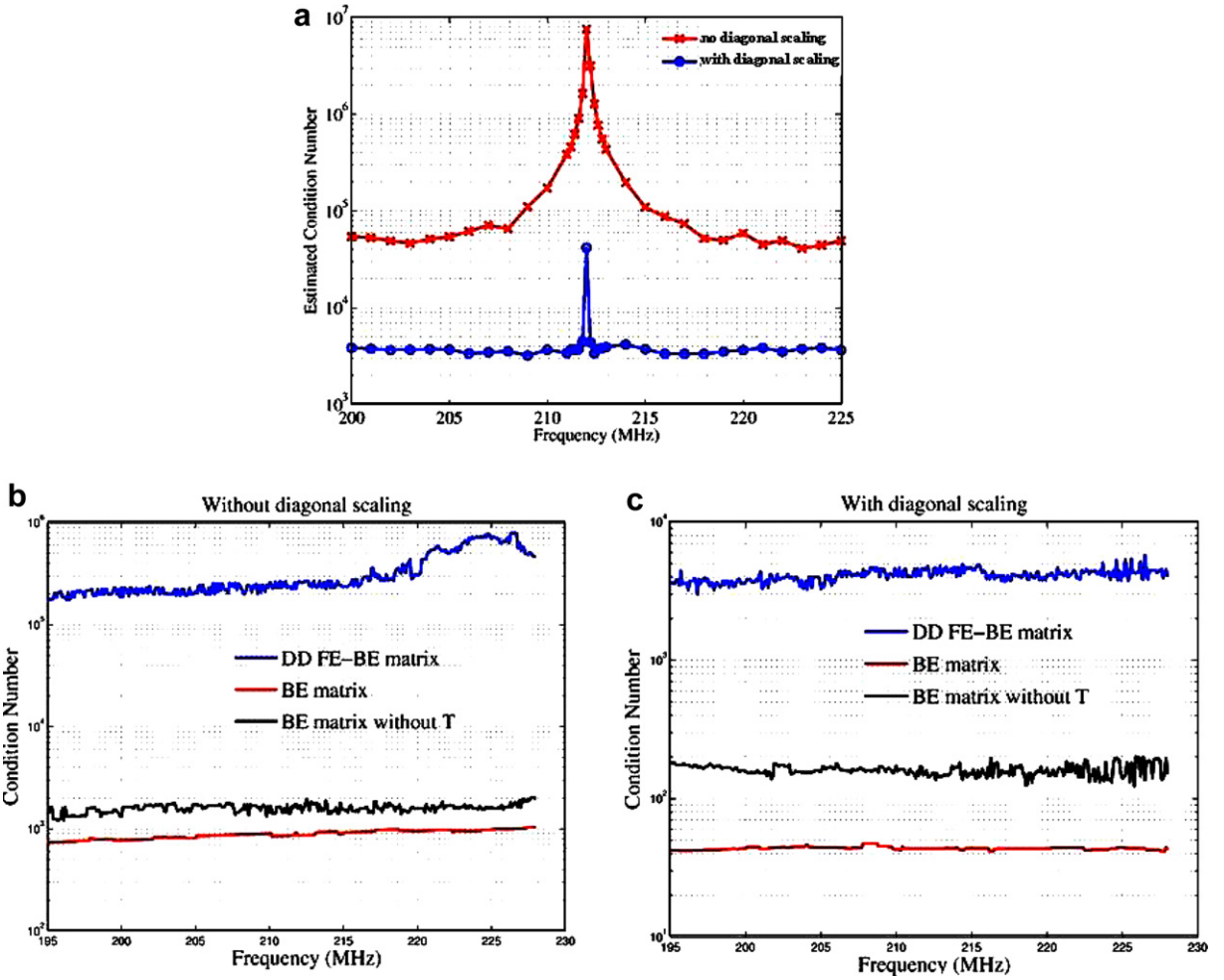

Fig. 4. Condition number of the system of equation in the neighborhood of the "internal" resonance. (a) Costabel's symmetric FEBI formulation. (b) Proposed approach without diagonal scaling. (c) Proposed approach with diagonal scaling.

modes) close to the unit circle rim around -1 and $+1$. Moreover, we observe that as the mesh size decreases, the accumulation points become more clustered around -1, 0 and 1.

8.2. Convergence studies

To study the convergence properties of the proposed method a dielectric sphere with progressively increasing mesh density is considered. The permittivity of the sphere is $\epsilon_r = 2$ and it has been facetized with unstructured triangles of the order of $h = \lambda_0/5$ at the coarsest mesh. The diameter of the sphere is $d = 4/3\lambda_0$. The BEM (truncation) boundary is placed right on-the-surface of the sphere. A series of progressively increasing mesh densities are constructed and simulated with the present method. The RMS error of the RCS of the sphere is considered and it is defined by

$$\text{RMS RCS error} = \sqrt{\frac{\int_0^{2\pi}\int_0^{\pi} |\sigma_{\text{DD–FE–BE}}(\theta,\phi) - \sigma_{\text{Mie}}(\theta,\phi)|^2 \mathrm{d}\theta\,\mathrm{d}\phi}{\int_0^{2\pi}\int_0^{\pi} |\sigma_{\text{Mie}}(\theta,\phi)|^2 \mathrm{d}\theta\,\mathrm{d}\phi}} \tag{8.1}$$

with $\sigma_{\text{DD–FE–BE}}$ and σ_{Mie} being the RCS of the proposed method and the analytical Mie series solution, respectively. It is noted that large number of angular sampling points are taken to ensure accurate error

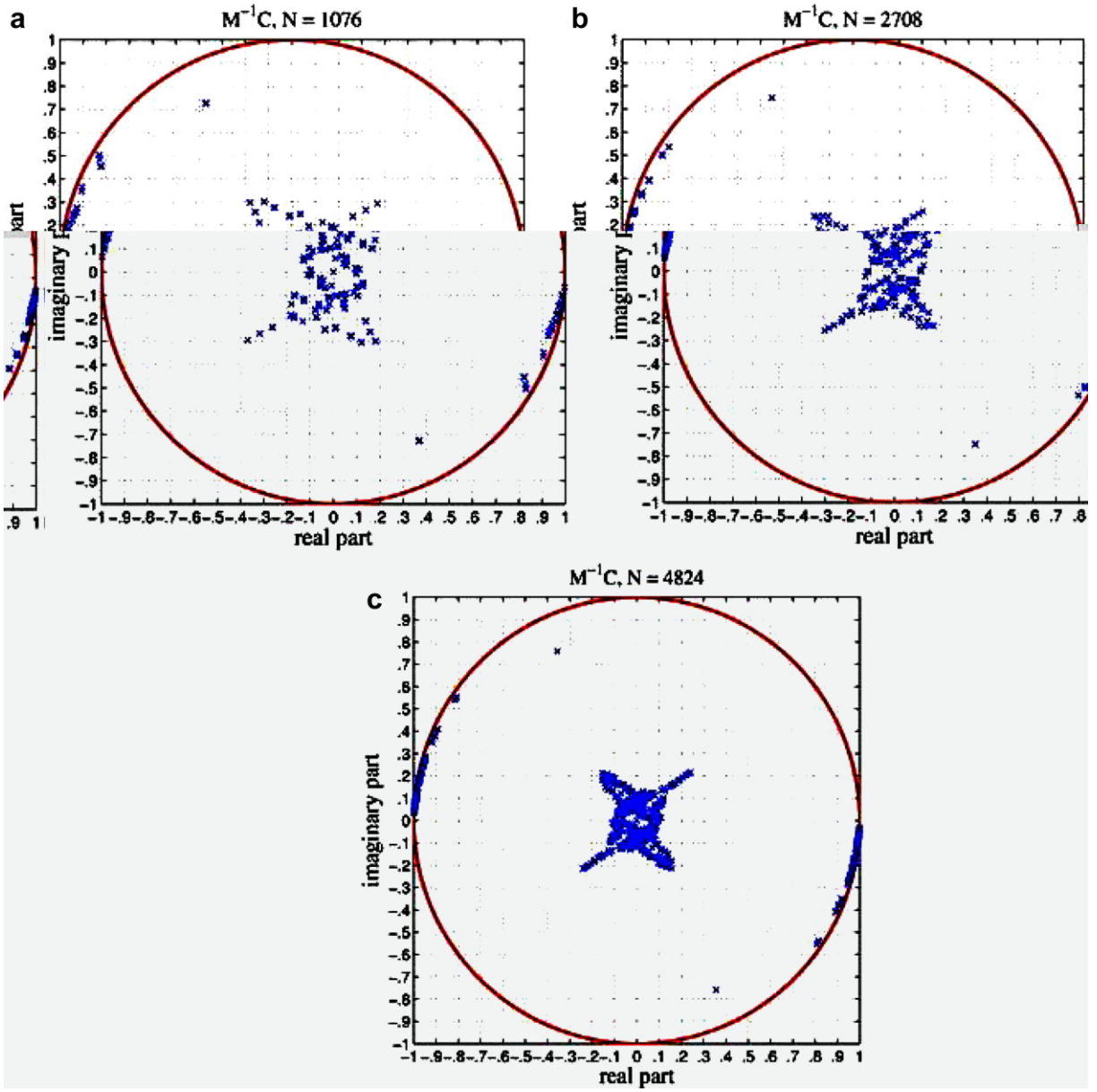

Fig. 5. Eigenvalue distribution of the coupling matrix $\mathscr{M}^{-1}\mathscr{C}$ for: (a) $N = 1076$ unknown problem. (b) $N = 2708$ unknown problem. (c) $N = 4824$ unknown problem. The frequency is kept constant at $f = 300$ MHz.

indication. The results of the study are presented in Fig. 6(a) where the RCS error is plotted versus the number of total unknowns. Note that the values obtained from the simulations (blue squares) are compared against with the second and first-order slope lines. This is done because the proposed implementation uses second-order FEM and first-order BEM basis functions. It is believed that in the coarse discretizations the discretization error of the FEM is predominant while for higher degrees of accuracy, the truncation error from BEM dominates and it is only first-order accurate. Thus, asymptotically the method is first-order accurate even though second-order FEM was utilized. The preconditioned CG convergence, with $\mathscr{M}_{\mathrm{DDB}}$ preconditioner, is plotted in Fig. 6(b) for the smallest and largest discretizations. The solid red line represents a discretization of $h = \lambda_0/5$ which results in 29,236 total unknowns. The solid blue line in the same figure represents the finest discretization of approximately $h = \lambda_0/20$ and 3,031,760 total unknowns. Despite the large

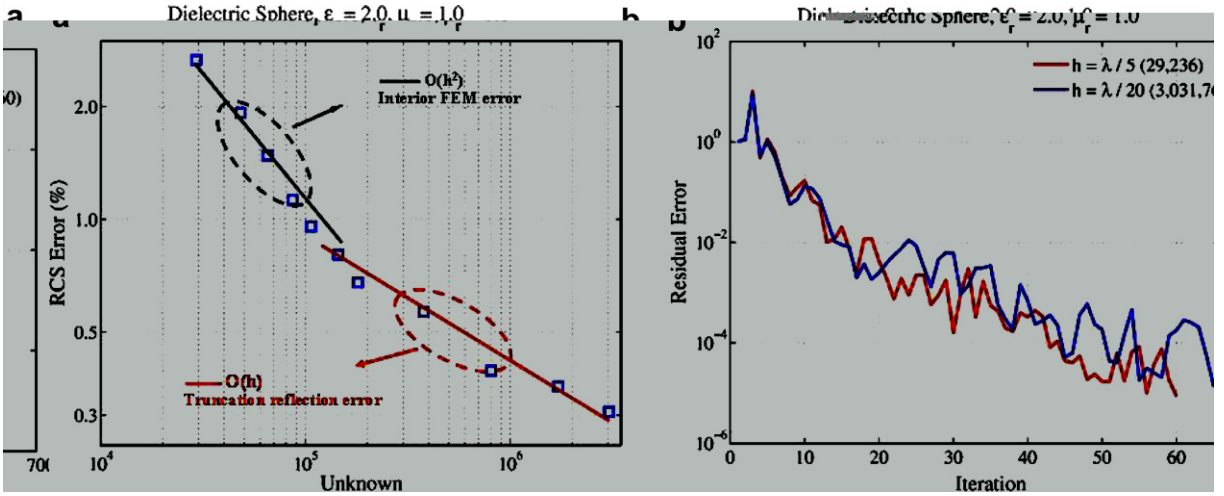

Fig. 6. Convergence properties of proposed DD–FEM–BEM (a) RCS error versus discretization. (b) History of the CG convergence for the smallest and largest discretization.

difference in both matrix size and discretization, the iterative solver behaves very well with a total iteration number only mildly dependent on the discretization size.

8.3. RCS from a generic battle ship

To demonstrate the versatility of the method, a more complicated example is considered, that is the scattering by a generic battleship. The geometry, dimensions, excitation and DD–FE–BEM computational domain are shown in Fig. 7. Notice that the BEM surface is quite complicated and non-convex. The ship is assumed to float in the free-space. The bistatic scattering patterns for 30 and 60 MHz are plotted in Fig. 8. Since the battleship is perfectly electric conducting an efficient PEC based EFIE BEM (MoM) solution can be employed. For both frequencies the comparisons between DD–FEM–BEM and MoM are very good. The DD–FE–BEM mesh was obtained from an initial discretization of $h = \lambda_0/5$ and through a goal-oriented h-version adaptive mesh refinements with estimated error of 0.05 [15].

The computational statistics of the DD–FE–BEM simulations for computing bistatics of a generic battleship at 10, 20 and 40 MHz are reported in Table 1. The CPU times reported are for matrix solution processes, which include the construction of the preconditioner, for different preconditioning strategies. However, the time required to construct the preconditioner is a very small fraction of the total solution times. Note that the number of iterations for DDB, AMS and MMS changed very little, particularly for the DDB case, even though the frequencies have been increased from 10 MHz to 40 MHz. This is consistent with the prediction indicated in Fig. 3. Furthermore, even though the number of iterations for the DD–FE–BEM to converge using the DDB preconditioner are small, the overall CPU times are significantly bigger than the other two preconditioners, AMS and MMS. Consequently, in practical computations, we simply employ either the AMS or the MMS preconditioners in solving the DD–FE–BEM matrix equations.

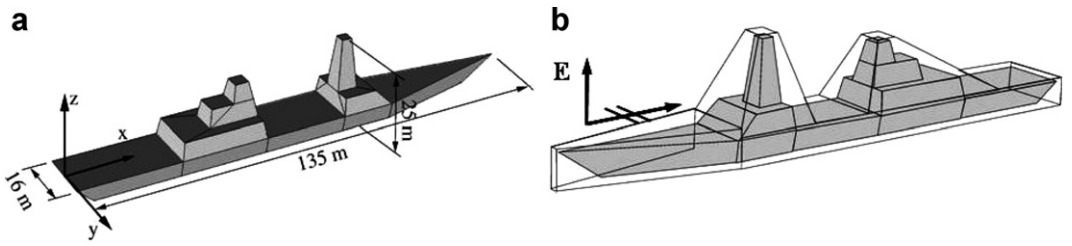

Fig. 7. A generic battle ship, (a) the geometry and the dimensions; and (b) the computational domain for the DD–FE–BEM.

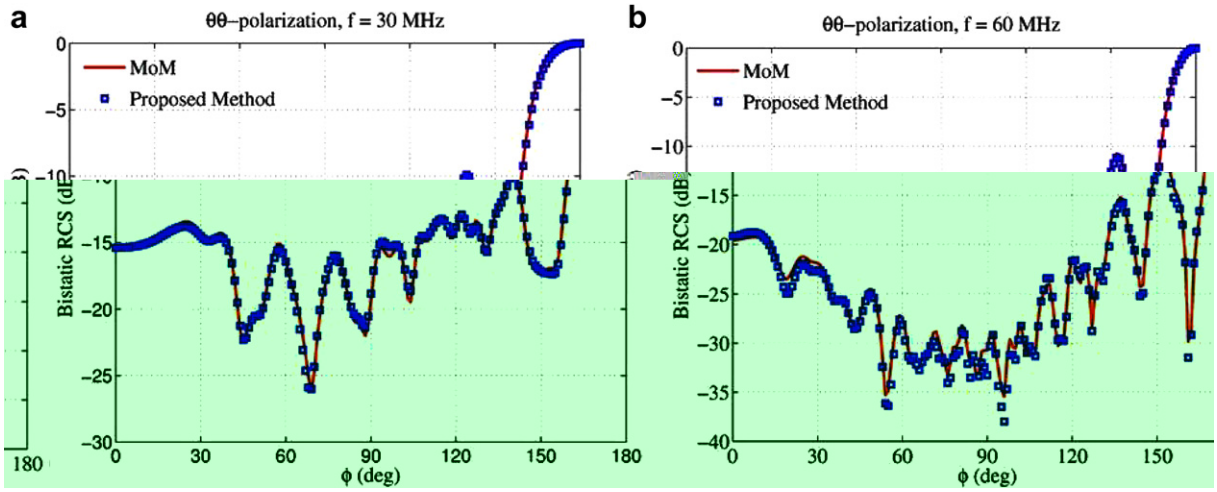

Fig. 8. The comparisons of the bistatic RCS results of DD–FE–BEM and the MoM. (a) $f = 30$ MHz and (b) $f = 60$ MHz.

Table 1
Computational statistics of the DD–FE–BEM for solving bistatic RCS of a generic battleship using three different preconditioning strategies

Frequency (MHz)	Memory (MB)	Unknowns		DDB		AMS		MMS	
		N_{FEM}	N_{BEM}	Iter.	CPU (hh:mm:ss)	Iter.	CPU (hh:mm:ss)	Iter.	CPU (hh:mm:ss)
10	196.5	102,006	10,680	87	00:57:34	106	00:02:11	43	00:01:05
20	553	320,444	27,036	97	03:15:22	133	00:06:56	67	00:04:27
40	2100	1,230,158	72,594	91	17:51:27	132	00:34:08	70	00:28:04

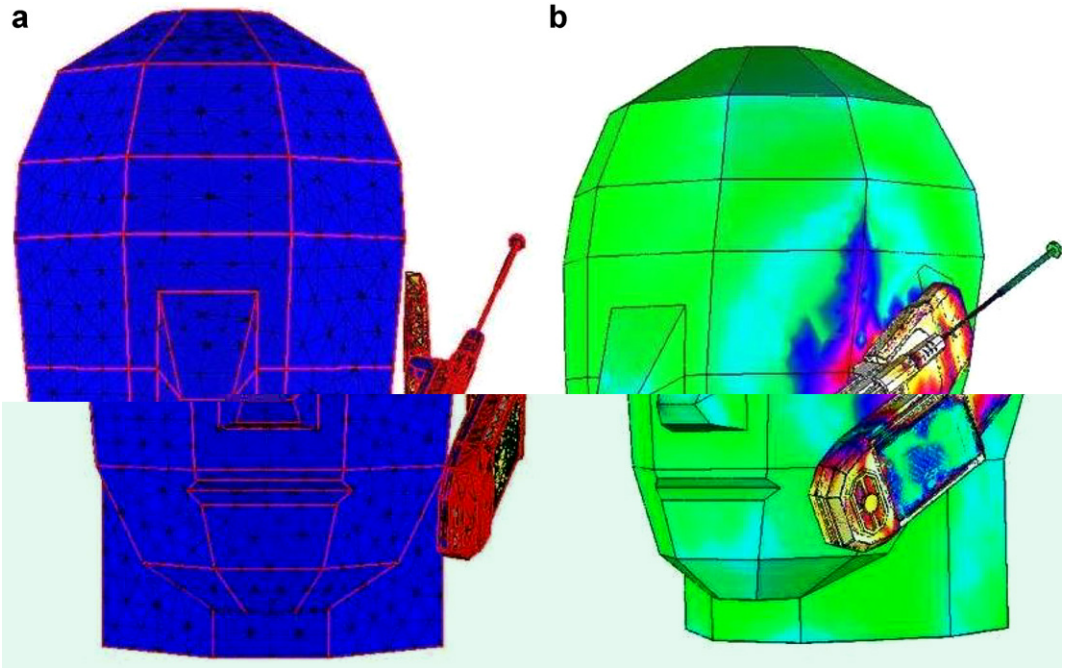

Fig. 9. A mobile phone in the vicinity of a human head. (a) The geometry and (b) the computed electric field distribution at $f = 1500$ MHz.

Table 2
Computational statistics of the DD–FE–BEM for modeling a commercial mobile phone in the vicinity of a human head

Frequency (MHz)	Memory (MB)	Unknowns		AMS		MMS	
		N_{FEM}	N_{BEM}	Iter.	CPU (hh:mm:ss)	Iter.	CPU (hh:mm:ss)
700	263	190,248	1464	225	00:03:44	72	00:01:46
1400	642	363,426	5778	188	00:07:47	90	00:05:19
2100	1300	717,980	12,390	171	00:16:57	359	00:59:02

8.4. Mobile phone in the vicinity of a human head

In Fig. 9, we show an example which consists of a mobile phone in the vicinity of a human head. For the material property of the head, $\epsilon_r = 45.93$ and $\sigma = 0.756$ were used, which were calculated according to Ref. [28]. Also included in Fig. 9 is the electric field distribution at $f = 1500$ MHz. Finally, we present the computational statistics in Table 2 of the DD–FE–BEM using both AMS and MMS preconditioners for modeling this example at three different frequencies, 700, 1400 and 2100 MHz. The number of iterations, for this example, varies more noticeably compared to the battleship example. This is mainly because for real-life engineering applications, the quality of the finite element tetrahedral mesh is usually not very satisfactory. Subsequently, the effectiveness of the preconditioners depends more on the variations of the mesh quality rather than on other factors. Moreover, at least for this example, it is not clear which preconditioner offers better performance. However, both of them perform quite reasonably well.

9. Conclusions

A new hybrid of FEM–BEM was proposed based on domain decomposition principles and the Robin-to-Robin map. Since the BEM portion of the variational statements utilizes the classical CombinedField Integral Equation (CFIE), the proposed method successfully mitigate the difficulties of internal resonances (the forbidden frequencies). The method is variational leading to symmetric systems, free of internal resonances and allows for non-conformal meshes on either sides of the truncation boundary. Probably among the most attractive features of the method is its modular nature that makes existing FEM and BEM codes easy to integrate into the hybrid FEM–BEM. In addition the method leads to a robust, stable and convergent algorithm with excellent iterative solver convergence properties when combined with the proposed DD based preconditioners. We have also provided simple physical interpretations of the proposed DD–FE–BE method and analyzed its convergence based on spherical harmonics using spherical truncation boundary to gain insights of the eigenspectrum of the coupling matrix. Both simple and real-life scattering problems confirmed the accuracy, robustness, stability and efficiency of the method.

References

[1] X. Yuan, Three-dimensional electromagnetic scattering from inhomogeneous objects by the hybrid moment and finite element method, IEEE Trans. Microwave Theory Tech. 38 (1990) 1053–1058.
[2] X. Yuan, D.R. Lynch, J.W. Strohbehn, Coupling of finite element and moment methods for electromagnetic scattering from inhomogeneous objects, IEEE Trans. Antennas Propag. 38 (8) (1990) 386–393.
[3] J.-M. Jin, J.L. Volakis, J.D. Collins, A finite-element-boundary integral method for scattering and radiation by two and three-dimensional structures, IEEE Antennas Propag. Magn. 33 (3) (1991) 22–32.
[4] D.J. Hoppe, L.W. Epp, J.-F. Lee, A hybrid symmetric FEM/MOM formulation applied to scattering by inhomogeneous bodies of revolution, IEEE Trans. Antennas Propag. 42 (1994) 798–805.
[5] J. Liu, J.-M. Jin, A novel hybridization of higher order finite element and boundary integral methods for electromagnetic scattering and radiation problems, IEEE Tran. Antennas Propag. 49 (12) (2001) 1794–1806.
[6] M. Costabel, Boundary Elements IX, Symmetric Methods for the Coupling of Finite Elements and Boundary Elements, Springer-Verlag, Berlin, 1987, pp. 411–420.
[7] R. Hiptmair, Symmetric coupling for eddy current problems, SIAM J. Numer. Anal. 40 (1) (2002) 41–65.
[8] R. Hiptmair, Coupling of finite elements and boundary elements in electromagnetic scattering, SIAM J. Numer. Anal. 41 (3) (2003) 919–944.

[9] M.N. Vouvakis, S.-C. Lee, K. Zhao, J.-F. Lee, A symmetric FEM-IE formulation with a single-level IE-QR algorithm for solving electromagnetic radiation and scattering problems, IEEE Trans. Antennas Propag. 52 (11) (2004) 3060–3070.
[10] S.-C. Lee, M.N. Vouvakis, K. Zhao, J.-F. Lee, Analyzing microwave devices using an IE-QRaccelerated symmetric febi, Int. J. Numer. Methods Eng. 203 (64) (2005) 528–546.
[11] T. Cwik, Coupling finite element and integral equation solutions using decoupled boundary meshes, IEEE Trans. Antennas Propag. 40 (1992) 496–1504.
[12] J. Liu, J.-M. Jin, A highly effective preconditioner for solving the finite element-boundary integral matrix equation of 3-d scattering, IEEE Trans. Antennas Propag. 50 (9) (2002) 1212–1221.
[13] B. Stupfel, A hybrid finite element integral equation domain decomposition method for the solution of 3-d scattering problem, J. Comput. Phys. 172 (2001) 451–471.
[14] S.-C. Lee, M. Vouvakis, J.-F. Lee, A non-overlapping domain decomposition method with non-matching grids for modeling large finite antenna arrays, J. Comput. Phys. 203 (2005) 1–21.
[15] D.K. Sun, Z.J. Cendes, J.-F. Lee, Adaptive mesh refinement h-version for solving multiport microwave devices in three dimensions, IEEE Trans. Magn. 36 (4) (2000) 1596–1599.
[16] W.C. Chew, J.-M. Jin, E. Michielssen, J. Song, Fast and Efficient Algorithms in Computational Electromagnetics, Artech House, Boston, MA, 2001.
[17] K. Zhao, M.N. Vouvakis, J.-F. Lee, The adaptive cross approximation algorithm for accelerated method of moments computations of EMC problems, IEEE Trans. Electromagn. Compat. (2005).
[18] M. Bebendorf, S. Rjasanow, Adaptive low-rank approximation of collocation matrices, Computing 70 (2003) 1–24.
[19] S.M. Seo, J.-F. Lee, A fast IE-FFT algorithm for solving PEC scattering problems, IEEE Trans. Magn. 41 (2005) 1476–1479.
[20] A. Buffa, R. Hiptmair, Galerkin boundary element methods for electromagnetic scattering, in: M. Aisworth et al. (Eds.), Topics in Computational Wave Propagation, Lecture Notes in Computational Science and Engineering, vol. 31, Springer, 2003, pp. 83–124.
[21] P.-A. Raviart, J.-M. Thomas, A Mixed Finite Element Method for second Order Elliptic Problems, Mathematical Aspects of Finite Element Methods, Lecture Notes of Mathematics, vol. 606, Springer Verlag, 1975.
[22] S.M. Rao, D.R. Wilton, A.W. Glisson, Electromagnetic scattering by surfaces of arbitrary shape, IEEE Trans. Antennas Propag. 30 (1982) 409–418.
[23] J.-C. Nédélec, Mixed finite elements in $\mathscr{R}^3$, Numer. Math. 35 (1980) 315–341.
[24] W.C. Chew, Waves and Fields in Inhomogeneous Media, Van Nostrand Reinhold, New York, 1990.
[25] D.K. Sun, J.F. Lee, Z.J. Cendes, Construction of nearly orthogonal Nedelec bases for rapid convergence with multilevel preconditioned solvers, SIAM J. Sci. Comput. 23 (4) (2001) 1053–1076.
[26] J.-F. Lee, D.K. Sun, Pmus (p-type multiplicative Schwarz) method with vector finite elements for modeling three-dimensional waveguide discontinuities, IEEE Trans. MTT 52 (2004) 864–870.
[27] B. Smith, P. Bjorstad, W. Gropp, Domain Decomposition, Cambridge University Press, 1996.
[28] Fcc tissue dielectric properties calculator. http://www.fcc.gov/fcc-bin/dielec.sh.